Arne P. Willner | Hans-Joachim Massonne | Uwe Ring
Masafumi Sudo | Stuart N. Thomson

P–T evolution and timing of a late Palaeozoic fore-arc system and its heterogeneous Mesozoic overprint in north-central Chile (latitudes 31–32° S)

Suggested citation referring to the original publication:
Geological Magazine 149 (2012) 2, pp. 177–207
DOI https://doi.org/10.1017/S0016756811000641
ISSN (print) 0016-7568
ISSN (online) 1469-5081

Geol. Mag. **149** (*2*), *2012, pp. 177–207. © Cambridge University Press 2011*
doi:10.1017/S0016756811000641

P–T evolution and timing of a late Palaeozoic fore-arc system and its heterogeneous Mesozoic overprint in north-central Chile (latitudes 31–32° S)

ARNE P. WILLNER*‡†, HANS-JOACHIM MASSONNE‡, UWE RING§, MASAFUMI SUDO¶ & STUART N. THOMSON‖

*Institut für Geologie, Mineralogie & Geophysik, Ruhr-Universität, D-44780 Bochum, Germany
‡Institut für Mineralogie und Kristallchemie, Universität Stuttgart, Azenbergstr. 18, D-70174 Stuttgart, Germany
§Department of Geological Sciences, University of Canterbury, Christchurch, New Zealand
¶Institut für Geowissenschaften, Universität Potsdam, Karl-Liebknechtstr. 24, D-14476 Potsdam, Germany
‖Department of Geosciences, University of Arizona, 1040 E. 4th St., Tucson, AZ 85721-0077, USA

(*Received* 30 May 2010; *accepted* 9 February 2011; *first published online* 16 August 2011)

Abstract – In the late Palaeozoic fore-arc system of north-central Chile at latitudes 31–32° S (from the west to the east) three lithotectonic units are telescoped within a short distance by a Mesozoic strike-slip event (derived peak *P–T* conditions in brackets): (1) the basally accreted Choapa Metamorphic Complex (CMC; 350–430 °C, 6–9 kbar), (2) the frontally accreted Arrayán Formation (AF; 280–320 °C, 4–6 kbar) and (3) the retrowedge basin of the Huentelauquén Formation (HF; 280–320 °C, 3–4 kbar). In the CMC, Ar–Ar spot ages locally date white-mica formation at peak *P–T* conditions and during early exhumation at 279–242 Ma. In a local garnet mica-schist intercalation (570–585 °C, 11–13 kbar) Ar–Ar spot ages refer to the ascent from the subduction channel at 307–274 Ma. Portions of the CMC were isobarically heated to 510–580 °C at 6.6–8.5 kbar. The age of peak *P–T* conditions in the AF can only vaguely be approximated at ≥ 310 Ma by relict fission-track ages consistent with the observation that frontal accretion occurred prior to basal accretion. Zircon fission-track dating indicates cooling below ∼ 280 °C at ∼ 248 Ma in the CMC and the AF, when a regional unconformity also formed. Ar–Ar white-mica spot ages in parts of the CMC and within the entire AF and HF point to heterogeneous resetting during Mesozoic extensional and shortening events at ∼ 245–240 Ma, ∼ 210–200 Ma, ∼ 174–159 Ma and ∼ 142–127 Ma. The zircon fission-track ages are locally reset at 109–96 Ma. All resetting of Ar–Ar white-mica ages is proposed to have occurred by *in situ* dissolution/precipitation at low temperature in the presence of locally penetrating hydrous fluids. Hence syn- and postaccretionary events in the fore-arc system can still be distinguished and dated in spite of its complex heterogeneous postaccretional overprint.

Keywords: Ar–Ar white-mica dating, zircon fission-track dating, accretionary prism, frontal accretion, basal accretion, thermal overprint, age resetting.

1. Introduction

The metamorphic basement of the entire coastal range of Chile from latitudes 28° S to 55° S is characterized by deep-seated coastal accretionary systems which, in central Chile, are of Late Carboniferous age. This basement provides an excellent natural laboratory to study processes at great depth that occurred within the corresponding subduction-accretion setting. Accretion processes in Chile have been studied for several decades (Aguirre, Hervé & Godoy, 1972; Gonzalez Bonorino, 1971; Hervé, 1988), with more recent accounts on the *P–T* evolution, geochronology and structural relationships within these accretionary systems in central Chile presented in Glodny *et al*. (2005, 2006), Willner (2005), Willner *et al*. (2004*a*, 2005), Willner, Gerdes & Massonne (2008) and Richter *et al*. (2007). After formation of the late Palaeozoic accretionary systems, continued activity at the Pacific margin up to present day means that study of these deep-seated accretionary systems is often hampered by variable later destruction and overprinting. For instance, in central Chile, between latitudes 34° and 42° S, early frontally accreted parts of the accretionary system were intruded by batholiths of the late Palaeozoic magmatic arc (Fig. 1a). Thus, these parts were invariably overprinted by a low pressure–high temperature (LP–HT) metamorphism coeval with ongoing accretion in deeper levels of the accretionary system (Willner, 2005; Willner *et al*. 2005). Metamorphic conditions and ages of the early accretionary processes at these latitudes, thus, remain unknown.

However, at the more northerly latitudes (30–32° S) the metamorphic basement occurs as scattered inliers within the Jurassic–Early Cretaceous arc, whereas the late Palaeozoic magmatic arc occurs considerably further east, intruding into a Carboniferous retrowedge basin (Fig. 1a). Here, the upper parts of the late Palaeozoic accretionary system show very low grade conditions and appear to represent more primary metamorphic conditions and ages related to accretion. For basement outcrops around lat. 31° S (Fig. 2), Rebolledo

†Author for correspondence: arne.willner@rub.de

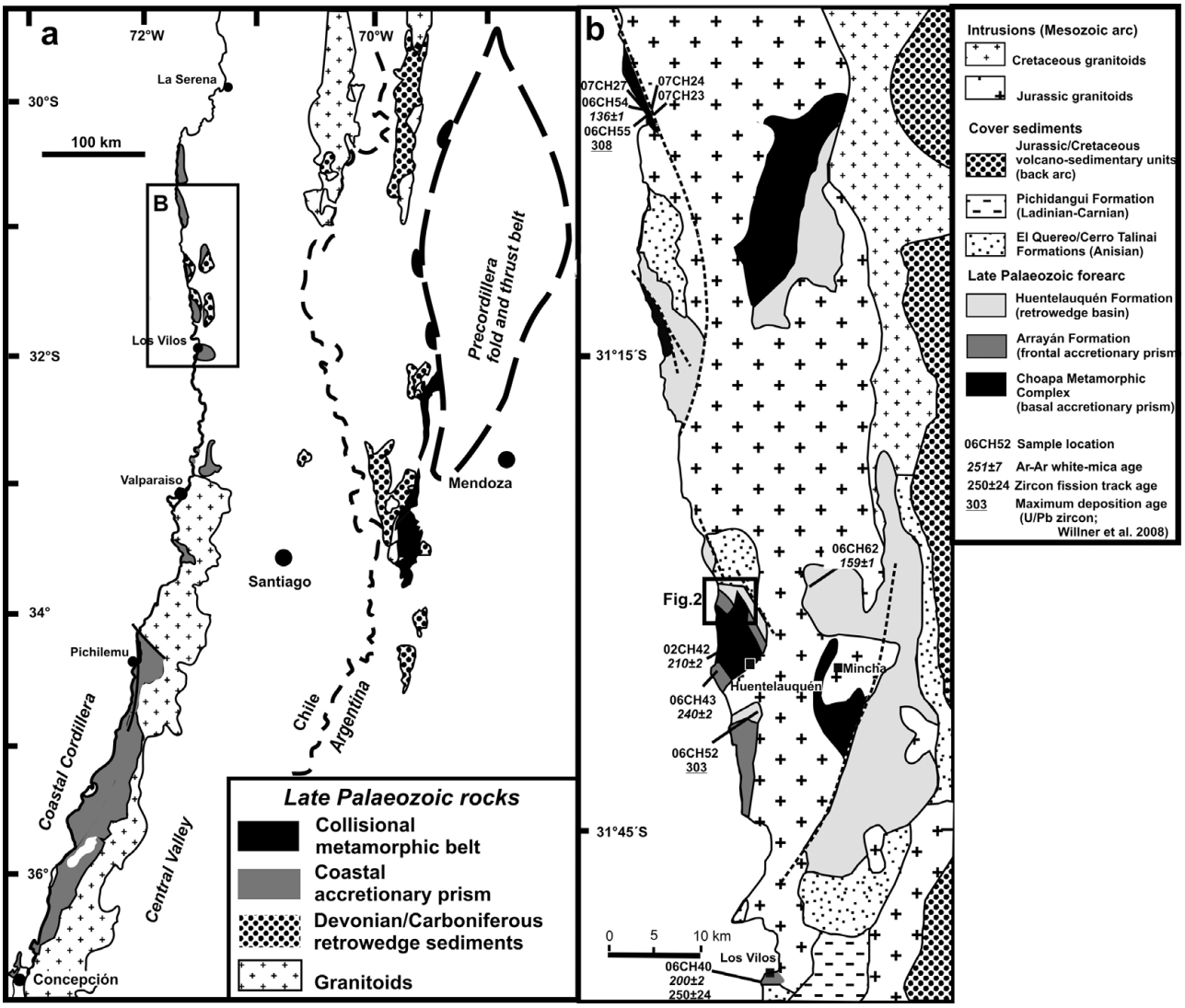

Figure 1. (a) Compilation of tectonic environments during late Palaeozoic times at lat. 29–37° S after Willner, Gerdes & Massonne (2008). (b) Geological map of the Chilean Coastal Range at lat. 31–32° S after Rivano & Sepúlveda (1983).

& Charrier (1994) inferred a late Palaeozoic age for the accretion process based on a biostratigraphical age for the sedimentary deposits accreted in the upper level of the fore-arc system and in analogy to the central Chilean accretionary systems further south. However, at 32° S, Irwin *et al*. (1988) derived Mesozoic K–Ar ages ranging between 140 Ma and 220 Ma for mineral concentrates from rocks of all basement units and attributed different age clusters to three successive episodes of deformation. Irwin *et al*. (1988) interpreted a first event around 200 Ma as corresponding to the formation of the accretionary system, being in contrast to much older ages in central Chile, south of 34° S. Furthermore, amphibolite-facies conditions were detected by Irwin *et al*. (1988), contrasting known high pressure–low temperature conditions (HP–LT) south of lat. 34° S (Willner, 2005). Also Godoy & Charrier (1991) observed hornblende overgrowing actinolite in metabasite at lat. 31° S, pointing to a local overprint at higher temperatures. It appears that our target region on the coast at lat. 31–32° represents a part of the accretionary systems where early original age relationships are still partly preserved, although some metamorphic and structural overprint as well as age resetting of a diverse nature and intensity does occur within a small distance.

The purpose of this paper is (1) to unravel the nature of the heterogeneous metamorphic imprint in different levels of the fore-arc system at lat. 31–32° S, (2) to date the peak metamorphic conditions related to accretion in the different levels, (3) to test age consistency with the model for the accretionary system proposed by Richter *et al*. (2007) and (4) to understand the nature of local metamorphic overprinting and (5) the contrasting local resetting of Ar–Ar and zircon fission-track (FT) ages. In a companion paper by Ring *et al*. (2011: this issue), prominent sinistral strike-slip shear zones overprinting the accretionary wedge structures are described in detail.

2. Geological setting

The metamorphic basement in north-central Chile at lat. 31–32° S shows various crustal levels of a fore-arc

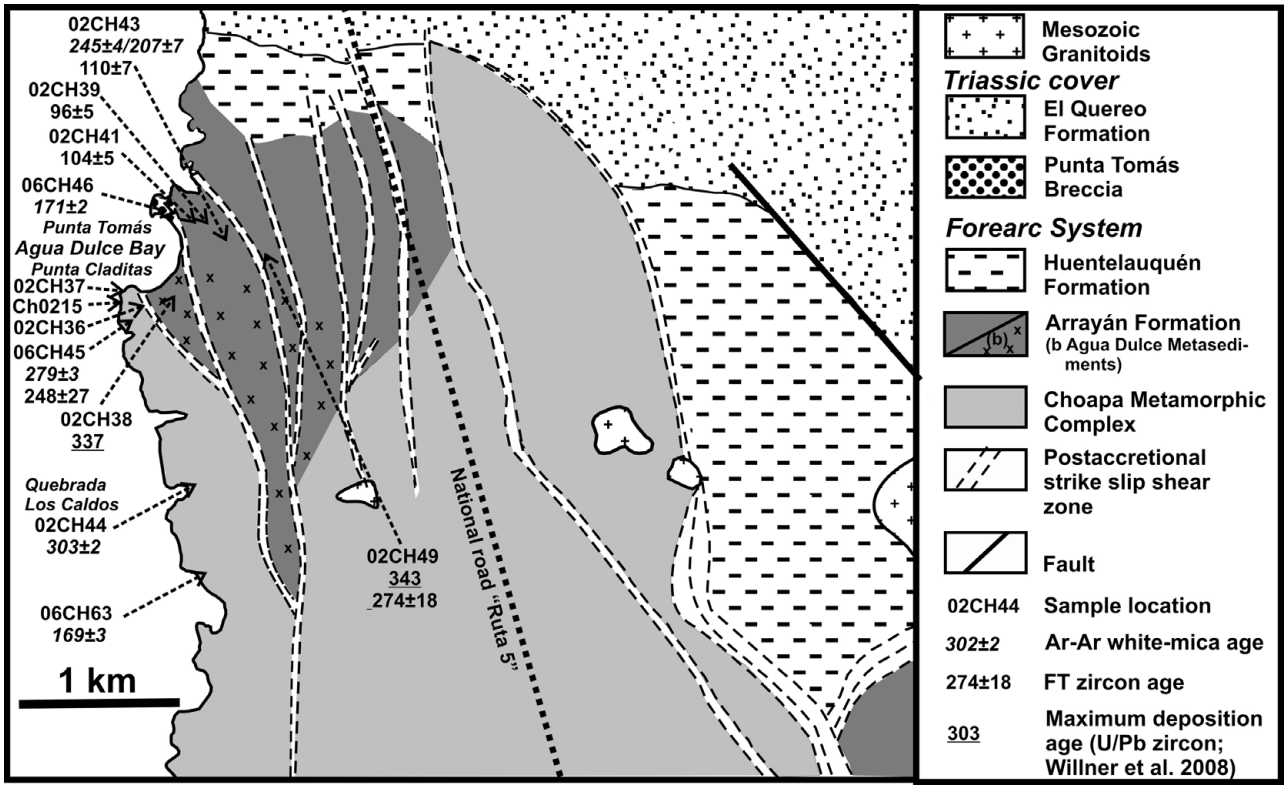

Figure 2. Detailed geological map of the Bahia Agua Dulce area modified after Rebolledo & Charrier (1994).

system, including an accretionary prism, which were telescoped to a short distance from each other by Mesozoic tectonic processes. These basement rafts form a chain of isolated inliers, mainly within the coastal batholith of the Jurassic magmatic arc (Fig. 1). Apart from numerous synonymous formation names and distinctions of sub-formations, three principle lithotectonic units of low to very-low grade metamorphic rocks (Figs 1b, 2) were distinguished in the late Palaeozoic fore-arc system by Rivano & Sepúlveda (1983, 1985), Thiele & Hervé (1984), Godoy (1984) and Rebolledo & Charrier (1994):

(1) The Choapa Metamorphic Complex (CMC) represents the structurally lowermost unit of the fore-arc system and comprises low grade metagreywackes with greenschist intercalations that are pervasively deformed by an originally sub-horizontal transposition foliation. The CMC has the same structural and lithological inventory as the Western Series south of 34° S that originated by basal accretion (Godoy 1984; Willner *et al*. 2005; Richter *et al*. 2007). Originally, the CMC was interpreted to represent metamorphic equivalents to the overlying Devonian–Lower Carboniferous Arrayán Formation (Rebolledo & Charrier 1994), but U–Pb dating of detrital zircon by Willner *et al*. (2008) showed that the maximum depositional age of the CMC is significantly younger (308 Ma). We also include the El Teniente Metamorphic Complex (Hervé *et al*. 2007) in the CMC owing to its similar lithology and similar style of deformation.

(2) The Arrayán Formation (AF) consists of very-low grade monotonous metagreywacke of turbiditic origin and metapelite. It shows similar structures to the frontally accreted Eastern Series, south of lat. 34° S (Richter *et al*. 2007), such as chevron folding of bedding planes and preserved orthostratigraphical continuity at outcrop scale including primary sedimentary structures (e.g. graded bedding). A Late Devonian–Early Carboniferous biostratigraphical age is assigned to the AF (Rebolledo & Charrier 1994 and references therein; their Puerto Manso Formation). On the basis of the youngest detrital magmatic zircon dated with the U–Pb system, Willner *et al*. (2008) derived a maximum depositional age of 343 Ma for the AF, consistent with its biostratigraphical age. This age is significantly older than that of the CMC and corroborates the general relationship for the Chilean accretionary prisms, as observed south of lat. 34° S, that basal accretion follows frontal accretion in time (Richter *et al*. 2007). We also include the 'Agua Dulce metaturbidites' of Rebolledo & Charrier (1994) into the AF because of a similar maximum depositional age of 337 Ma (Willner *et al*. 2008). These metaturbidites form a more strongly deformed structural base of the AF, where sub-horizontal folds of a second folding event continuously become tighter, grading into the transposition foliation that characterizes the CMC. The continuous transition between the AF and CMC had already been recognized by Godoy (1984), who correlated it with the classic transition localities at lat. 35–36° S (Richter *et al*. 1977).

(3) The Huentelauquén Formation (HF), unconformably overlying the AF, is a heterogeneous sedimentary sequence of metagreywacke with shale and

conglomerate intercalations at its base overlain by thick shelf deposits comprising polymict conglomerate, platform carbonate and metasandstone. Rivano & Sepúlveda (1983, 1985) assigned a Late Carboniferous to Permian biostratigraphic age to the HF (see also Charrier, Pinto & Rodríguez, 2007 and references therein). U–Pb dating of magmatic zircon in pebbles of the conglomerate yielded a maximum age of deposition at 303 Ma for the HF (Willner *et al*. 2008), consistent with its biostratigraphical age. Deposition was apparently concomitant with that of the CMC (maximum depositional age 308 Ma). Charrier, Pinto & Rodríguez (2007) described detritus supply from the NW and, hence, deposition concomitant with an emerging accretionary prism, whereas Willner *et al*. (2008) dated granite and rhyolite pebbles that derived from a nearby emerging area with a coeval magmatic source further east. Thus, the HF must have been deposited on a shelf within a retrowedge position as already inferred by Thiele & Hervé (1984). An unconformity observed within the HF (Charrier, Pinto & Rodríguez, 2007) also suggests pronounced tectonic activity during its deposition. The concomitant late Palaeozoic arc intruded the retrowedge basin further to the east of the study area at 310–256 Ma (Elqui-Limari batholith; Mpodozis & Kay 1992; Pankhurst, Millar & Hervé, 1996).

The Lower Triassic El Quereo Formation (EQF) unconformably overlies the rocks of the fore-arc system with a prominent breccia (Punta Tomás Breccia) at its base (Charrier, Pinto & Rodríguez, 2007). This formation consists of fine- to coarse-grained sandstones with pelitic and conglomeratic intercalations. Deposition started within a deltaic environment and later graded into a more distal greywacke/shale succession. The fossiliferous levels of the EQF indicate an Anisian age (Charrier, Pinto & Rodríguez, 2007 and references therein) and they are overlain by the Pichidangui Formation (Ladinian–Carnian), which includes bimodal volcanic deposits related to extension.

The oldest intrusion ages (Rb–Sr whole-rock isochron dating) obtained by Irwin *et al*. (1988) at 31° S are 220 ± 20 Ma for a gabbro and 200 ± 10 Ma for a monzogranite documenting the end of the accretion process at the same time as in north-central Chile (Willner *et al*. 2005) and south-central Chile (Glodny *et al*. 2006). This magmatic event is concomitant with an extensional event, with ubiquitous opening of a series of NNW–SSE-trending basins in an en échelon pattern in central Chile (Charrier, Pinto & Rodríguez, 2007 and references therein). The isolated outcrops of the metamorphic basement and relics of their Triassic cover mainly constitute inliers within Jurassic batholiths with mostly intrusive but also tectonic contacts, although some intrusive contacts with Cretaceous plutons are also observed in the eastern part of the study area.

During Jurassic to Middle Cretaceous times (starting around 200 Ma), an extensive N–S-trending magmatic arc developed near the present coast with extensive marine back-arc basins further inland (Parada *et al*. 2007). There is no unconformity between Triassic and Jurassic deposits. Subduction-related extensional deformation concurrent with mostly bimodal volcanism and calcalkaline plutonic activity, with progressively more mantle participation, dominated the entire Mesozoic history within a 1200 km long magmatic belt (Parada *et al*. 2007 and references therein). Furthermore, conspicuous bimodal dyke intrusions are ubiquitous within all rocks of the metamorphic basement and the Triassic inliers. K–Ar dating of hornblende in mafic dykes yielded ages of 133–213 Ma (Irwin *et al*. 1988). The Atacama Fault system developed during Jurassic times, with strike-slip activity mainly bound to the magmatic arc itself. Back-arc basins were closed during a Middle Cretaceous compressive event (Arancibia, 2004), and during Late Cretaceous times the magmatic arc moved further east without the development of back-arc basins.

3. Analytical and geothermobarometric methods

We selected representative rock samples from distinct parts of the outcrop areas (Figs 1, 2) for petrological and geochronological studies. The qualitative modal composition of these samples and their locations are given in Table 1. Mineral compositions were obtained using a CAMECA SX 100 electron microprobe with five wavelength-dispersive systems at Universität Stuttgart, Germany. Operating conditions were an acceleration voltage of 15 kV, a beam current of 15 nA, 20s counting time per element on both the peak and the background, and a defocused beam of 8 μm in order to avoid loss of alkalis in mica and amphibole. We used natural minerals, glasses and pure oxides as standards. The PAP correction procedure provided by Cameca was used for matrix correction. Representative analyses and structural formulae of minerals used for *P–T* calculations, together with the calculation procedure of the structural formulae, are presented in Table 2. Further data are available as supplementary data tables in the online Appendix at http://journals.cambridge.org/geo and upon request to the first author. Abbreviations of minerals and end-member components in this paper are: Ab – albite, Am – amphibole, Bt – biotite, Cl – chlorite, Ep – epidote, Gt – garnet, Im – ilmenite, Kf – potassic feldspar, Lw – lawsonite, Mt – magnetite, Pg – paragonite, Pl – plagioclase, Qz – quartz, Rt – rutile, Tt – titanite, V – H_2O as hydrous fluid, Wm – potassic white-mica.

Whole-rock analyses of major elements were achieved at Ruhr-Universität Bochum with a Philips PW 2400 X-ray fluorescence spectrometer on glass discs. Selected data are presented in Table 3.

^{40}Ar–^{39}Ar dating was performed in the ^{40}Ar–^{39}Ar geochronology laboratory at Universität Potsdam after neutron activation of polished sections (1 cm diameter) at the Geesthacht Neutron Facility (GeNF) of the GKSS in Geesthacht, Germany. The polished thick-sections

Table 1. Assemblages in the studied rock types, their peak *P–T* conditions, ages and locations

Sample	Am	Gt	Ep	Cl	Wm	Pg	Bt	Qz	Ab	Pl	Kf	Rt	Im	Tt	Peak *P–T* conditions		Maximum deposition age (Ma)** U–Pb zircon	Ar–Ar age (Ma) white-mica	FT age (Ma) zircon	Location	Coordinates	
															P (kbar)	T (°C)					latitude (S)	longitude (W)
Choapa Complex																						
Metapsammopelite																						
CH02150				x	x			x	x				x		4–8	< 450				Punta Claditas	31°31′14.3″	71°34′31.2″
06CH45				x	x			x	x			x	x		4–8	< 450		242–279	248 ± 27	Punta Claditas	31°31′14.9″	71°34′31.2″
02CH36		x*		x	x			x				x	x	(x)	4–8	> 450				Punta Claditas	31°31′14.3″	71°34′30.5″
06CH54			x	x	x		x	x	x	x			x	x	4–8	> 500	308	127–143		Playa La Cebada	30°58′14.43″	71°39′04.6″
07CH27					x		x	x	x				x		4–8	> 450				E Playa La Cebada	30°58′14.43″	71°38′40″
Garnet mica-schist																						
02CH44		x	x	x	x			x				x		(x)	11–13	> 570–585		198–307		Quebrada Los Caldos	31°31.91′	71°34.27′
Metabasite																						
07CH24	x			x			x	x	x					x	< 4.5	< 380				E Playa La Cebada	30°58′14.40″	71°38′31″
02CH37	x		x	x	x			x	x					x	6.2	353				Punta Claditas	31°31′14.3″	71°34′31.2″
07CH23	x		x	x				x	x	x			x		> 6.0	> 480				E Playa La Cebada	30°58′14.33″	71°38′40″
06CH55	x			x				x		x		x	x		> 6.0	> 480				Playa La Cebada	30°58′14.43″	71°39′04.6″
06CH63	x		x	x	x			x	x		x	x		(x)	6.7	575		169 ± 3		Quebrada Maitencillo	31°32′28.5″	71°33′57.7″
06CH42	x		x	x	x	x						x		(x)	8.3	518		188 ± 2 /200 ± 2		N Rio Choapa estuary	31°35′42″	71°34′49.9″
Arrayán Formation																						
Metapsammopelite																						
06CH40				x	x			x	x		x		x	x	4.0–6.0	280–320		200 ± 2	250 ± 24	SW of Los Vilos	31°55′35.5″	71°31′07.1″
06CH43				x	x			x	x		x		x		4.0–6.0	280–320		227–251		N Rio Choapa estuary	31°35′22.1″	71°34′17.7″
02CH38				x	x		x	x	x		x		x		4.0–6.0	280–320	337			E´Punta Claditas	31°31′06″	71°34′30″
06CH46				x	x			x	x		x		x		4.0–6.0	280–320		165–174		Punta Tomás	31°30′32″	71°34′15″
02CH41				x	x			x	x							280–320			104 ± 5	E Playa Agua Dulce	31°30′42″	71°34′10″
02CH39				x	x			x	x				x			280–320			96 ± 5	E Playa Agua Dulce	31°30′50″	71°34′05″
02CH43				x	x			x	x				x			280–320		244 ± 4 /207 ± 7	109 ± 7	E Playa Agua Dulce	31°30′52″	71°34′00″
02CH49				x	x			x	x				x			280–320	343		274 ± 18	E Playa Agua Dulce	31°31.44′	71°34.05′
Huentelauquén Fm																						
Metapsammopelite																						
02CH62				x	x			x	x		x					280–320		159 ± 1		Ermita Padre Hurtado	31°29′04.7″	71°33′46.9″
Metaconglomerate																						
06CH52				x	x		x	x	x		x				3.0–4.5	< 350	303	101–175		Quarry S Huentelauquén	31°35.08′	71°31.92′

*garnet pseudomorph; (x) retrograde; **Willner *et al*. (2008).

Table 2. Representative mineral analyses and mineral compositions calculated with PERPLE_X for comparison

	Actinolite						Hornblende				
Amphibole	02CH37	02CH42 core	06CH55 core	07CH23 core	07CH24	MORB calculated	06CH63 rim	02CH42 rim	06CH55 rim	07CH23 rim	MORB calculated
SiO_2	51.04	54.25	52.99	55.83	54.80		43.95	44.66	45.45	43.38	
Al_2O_3	5.58	2.97	1.86	0.95	1.54		14.11	13.72	9.70	13.16	
TiO_2	0.14	0.05	0.03	0.02	0.03		0.43	0.39	0.40	0.59	
Fe_2O_3	6.98	4.00	7.76	5.03	3.58		5.04	2.53	12.02	5.39	
FeO’	8.44	5.87	2.80	5.52	6.37		8.01	10.55	1.15	10.61	
MgO	13.57	17.81	18.59	18.73	18.08		11.60	11.34	14.71	11.12	
CaO	10.56	12.10	11.98	12.52	12.47		10.48	10.93	10.70	12.06	
BaO	0.00	0.00	0.00	0.00	0.00		0.00	0.00	0.04	0.00	
K_2O	0.19	0.06	0.08	0.02	0.02		0.28	0.32	0.17	0.21	
Na_2O	1.15	0.54	0.28	0.16	0.15		2.51	2.53	1.18	1.87	
MnO	0.27	0.15	0.15	0.18	0.20		0.16	0.13	0.26	0.21	
H_2O’	2.09	2.13	2.10	2.16	2.12	(350 °C/ 4 kbar)	2.05	2.05	2.06	2.05	(500°C/ 7kbar)
Sum	100.04	99.92	98.69	101.15	99.42		98.63	99.15	97.96	100.80	
Si	7.332	7.634	7.550	7.767	7.762	7.920	6.432	6.533	6.613	6.335	6.080
Al^{IV}	0.668	0.366	0.312	0.156	0.238	0.080	1.568	1.467	1.388	1.665	1.920
Sum	8.000	8.000	7.862	7.923	8.000	8.000	8.000	8.000	8.000	8.000	8.000
Al^{VI}	0.276	0.126	0.000	0.000	0.020	0.680	0.866	0.899	0.276	0.600	1.040
Ti	0.016	0.006	0.003	0.002	0.003	0.000	0.048	0.042	0.044	0.065	0.000
Mn	0.032	0.017	0.018	0.022	0.025	0.000	0.020	0.016	0.033	0.026	0.000
Fe3+	0.755	0.424	0.833	0.527	0.382	0.000	0.555	0.279	1.316	0.592	0.000
Fe2+	1.014	0.691	0.334	0.642	0.754	1.560	0.980	1.291	0.140	1.296	1.430
Mg	2.906	3.736	3.950	3.884	3.817	2.760	2.531	2.473	3.191	2.421	2.530
Sum	13.000	13.000	13.000	13.000	13.000	13.000	13.000	13.000	13.000	13.000	13.000
Ca	1.626	1.824	1.830	1.866	1.893	1.360	1.643	1.714	1.669	1.887	1.920
Ba	0.000	0.000	0.000	0.000	0.000	0.000	0.000	0.000	0.002	0.000	0.000
Na	0.320	0.148	0.076	0.044	0.042	0.640	0.713	0.718	0.334	0.530	1.040
K	0.035	0.010	0.014	0.004	0.004	0.000	0.052	0.059	0.032	0.039	0.000
Sum	1.980	1.981	1.920	1.914	1.938	2.000	2.408	2.491	2.037	2.456	2.960
OH	2.000	2.000	2.000	2.000	2.000	2.000	2.000	2.000	2.000	2.000	2.000

Proportion of cations is based on the sum of cations = 13 except for Ca, Na and K for estimation of Fe3+ and on 46 negative charges

Table 2. continued

Garnet	02CH44 core	rim	02CH44 calc.
SiO_2	36.75	37.57	
Al_2O_3	20.39	21.01	
TiO_2	0.24	0.11	
Fe_2O_3	1.52	1.18	
FeO’	27.89	30.75	
MnO	4.57	0.22	
MgO	1.13	3.66	
CaO	7.90	6.26	(600 °C/ 12 kbar)
Sum	100.53	100.89	
Si	5.918	5.934	3.000
Alt	0.083	0.066	
Sum	6.000	6.000	
Alo	3.788	3.846	2.000
Fe3+	0.184	0.141	
Ti	0.029	0.013	
Sum	4.000	4.000	
Fe2+	3.757	4.062	1.950
Mn	0.623	0.029	0.060
Ca	1.363	1.059	0.620
Mg	0.271	0.863	0.370
Sum	6.014	6.013	3.000

Feldspar	07CH23 core	rim	06CH45	06CH63	06CH63
SiO_2	68.45	59.16	65.25	64.13	68.14
Al_2O_3	19.56	26.01	19.77	18.81	19.30
FeO	0.14	0.32	0.11	0.04	0.16
CaO	0.06	7.50	0.25	0.00	0.32
BaO	0.00	0.01	0.00	1.69	0.00
Na_2O	11.80	7.31	11.36	0.19	12.01
K_2O	0.05	0.04	0.02	14.45	0.06
Sum	100.09	100.35	96.78	99.33	100.01
Si	2.989	2.633	2.952	2.989	2.986
Alt	0.011	0.367	0.048	0.011	0.014
Sum	3.000	3.000	3.000	3.000	3.000
Alo	0.996	0.998	1.006	1.023	0.982
Fe	0.005	0.012	0.004	0.002	0.006
Mn	0.001	0.000	0.000	0.000	0.000
Sum	1.003	1.010	1.010	1.025	0.989
Ca	0.003	0.358	0.012	0.000	0.015
Ba	0.000	0.000	0.000	0.031	0.000
Na	0.999	0.631	0.997	0.017	1.020
K	0.003	0.002	0.001	0.859	0.003
Sum	1.005	0.991	1.010	0.908	1.038
O’	8.000	8.000	8.000	8.000	8.000
Albite	99.44	63.66	98.68	1.92	98.25
Anorthite	0.27	36.11	1.19	0.00	1.43
Orthoclase	0.29	0.21	0.13	94.69	0.32

Cations based on 48 negative charges including 10 cations in the tetrahedral and octahedral site to calculate Fe3+
Normalization on the basis of 16 negative charges

were wrapped in commercial Al foils and set into the drilled holes of the 99.999 % pure Al sample holder. The package was Cd-shielded and irradiated with fast neutrons with a flux of 1×10^{12} n/cm^2/s for 96 hours. The Fish Canyon Tuff sanidine (age 27.5 Ma; Uto *et al*. 1997; Ishizuka, Yuasa & Uto, 2002) was used as a flux monitor during irradiation to obtain the J values, which reflect the degree of neutron activation for the irradiated samples. K_2SO_4 and CaF_2 crystals were also irradiated to correct interference of

Table 2. continued

White-mica	07CH37 core	02CH42 core	02CH42 rim	06CH63 rim	MORB calc.	MORB calc.	CH21503 core	06CH45 core	06CH45 core calc.	06CH45 core calc.	02CH44 core	02CH44 rim	02CH44 calc.	06CH54 core	06CH43 metam.	06CH43 detrital	06CH40 metam.	06CH40 detrital	06CH46 metam.	06CH52c metam.	06CH52 detrital
SiO_2	48.69	49.49	48.30	46.04			47.40	46.47			48.48	47.21		49.92	49.42	47.48	48.31	46.19	49.79	47.56	49.30
Al_2O_3	27.56	29.54	31.86	31.02			32.10	28.56			29.81	31.51		31.85	28.85	29.01	29.12	34.21	27.68	31.75	29.66
TiO_2	0.24	0.32	0.34	0.11			0.20	0.29			0.37	0.46		0.27	0.01	0.22	0.41	0.52	0.27	0.25	0.15
Fe_2O_3	0.67	0.00	0.00	0.98			0.00	0.93			0.00	0.00		0.00	0.00	0.45	0.27	0.00	0.00	0.00	0.00
FeO’	3.15	2.13	2.04	1.72			2.02	2.35			3.36	3.02		1.21	4.37	3.98	2.98	1.76	3.48	2.42	3.70
MgO	3.01	2.92	2.27	2.25			1.32	2.61			2.23	1.57		1.08	1.21	1.87	2.68	1.05	2.77	0.96	1.35
MnO	0.00	0.02	0.00	0.00			0.05	0.01			0.01	0.05		0.00	0.00	0.00	0.00	0.00	0.00	0.00	0.06
CaO	0.07	0.30	0.02	0.02			0.00	0.00			0.00	0.03		0.05	0.00	0.00	0.00	0.00	0.00	0.00	0.10
BaO	0.25	0.39	0.76	0.56			0.18	0.23			0.28	0.29		0.26	0.21	0.18	0.23	0.12	0.20	0.14	0.00
Na_2O	0.23	0.45	1.02	0.19			0.41	0.35			0.91	0.57		0.29	0.19	0.35	0.50	0.69	0.50	0.13	0.11
K_2O	10.45	8.49	8.84	9.84			9.88	10.48			9.26	9.57		9.69	10.26	10.16	9.46	10.24	10.13	10.36	10.56
H_2O’	4.41	4.51	4.53	4.37	(350°C/	(500°C/	4.44	4.31	(350°C/	(550°C/	4.46	4.45	(600°C/	4.55	4.44	4.38	4.44	4.47	4.45	4.43	4.47
Sum	98.89	98.56	99.97	97.09	4 kbar)	7 kbar)	97.98	96.59	7 kbar)	6.5 kbar)	99.16	98.74	13 kbar)	99.17	98.95	98.10	98.40	99.26	99.28	98.02	99.46
Si	3.311	3.292	3.199	3.157	3.310	3.160	3.200	3.235	3.290	3.130	3.256	3.183	3.250	3.293	3.341	3.253	3.261	3.095	3.352	3.220	3.309
Alt	0.689	0.708	0.801	0.843	0.690	0.840	0.800	0.765	0.710	0.870	0.744	0.817	0.750	0.707	0.659	0.747	0.739	0.905	0.648	0.780	0.691
Sum	4.000	4.000	4.000	4.000	4.000	4.000	4.000	4.000	4.000	4.000	4.000	4.000	4.000	4.000	4.000	4.000	4.000	4.000	4.000	4.000	4.000
Alo	1.520	1.608	1.687	1.665	1.690	1.830	1.754	1.578	1.720	1.780	1.615	1.687	1.750	1.769	1.640	1.596	1.577	1.797	1.549	1.754	1.656
Ti	0.012	0.016	0.017	0.006			0.010	0.015			0.019	0.023		0.014	0.001	0.012	0.021	0.026	0.013	0.013	0.008
Fe3+	0.034	0.000	0.000	0.051			0.000	0.049			0.000	0.000		0.000	0.000	0.023	0.014	0.000	0.000	0.000	0.000
Fe2+	0.179	0.119	0.113	0.099	0.090	0.040	0.114	0.137	0.140	0.070	0.189	0.171	0.090	0.067	0.247	0.228	0.168	0.099	0.196	0.137	0.208
Mn	0.000	0.001	0.000	0.000			0.003	0.000			0.000	0.003		0.000	0.000	0.000	0.000	0.000	0.000	0.000	0.003
Mg	0.305	0.290	0.224	0.230	0.220	0.130	0.133	0.270	0.140	0.150	0.223	0.158	0.160	0.106	0.122	0.191	0.270	0.105	0.278	0.097	0.135
Sum	2.050	2.034	2.040	2.050	2.000	2.000	2.013	2.050	2.000	2.000	2.046	2.042	2.000	1.955	2.009	2.050	2.050	2.028	2.036	2.000	2.010
Ba	0.007	0.010	0.020	0.015			0.005	0.006			0.007	0.008		0.007	0.006	0.005	0.006	0.003	0.005	0.004	0.000
Ca	0.005	0.022	0.002	0.001			0.000	0.000			0.000	0.002		0.003	0.000	0.000	0.000	0.000	0.000	0.000	0.007
Na	0.031	0.059	0.131	0.025	0.020	0.080	0.053	0.047	0.060	0.120	0.118	0.075	0.080	0.037	0.025	0.046	0.065	0.089	0.065	0.018	0.014
K	0.907	0.721	0.747	0.861	0.980	0.920	0.851	0.931	0.940	0.880	0.793	0.823	0.920	0.815	0.885	0.888	0.814	0.876	0.870	0.895	0.904
Sum	0.949	0.811	0.899	0.902	1.000	1.000	0.909	0.985	1.000	1.000	0.919	0.908	1.000	0.863	0.915	0.940	0.886	0.968	0.940	0.917	0.926
OH	2.000	2.000	2.000	2.000	2.000	2.000	2.000	2.000	2.000	2.000	2.000	2.000	2.000	2.000	2.000	2.000	2.000	2.000	2.000	2.000	2.000
O’	9.988	9.921	9.960	9.951	10.000	10.000	9.957	9.993	10.000	10.000	9.963	9.959	10.000	9.936	9.960	9.970	9.943	9.986	9.973	9.960	9.966

The proportion of cations is based on 21 negative charges neglecting the interlayer cations; the sum of octahedrally coordinated cations is set at 2.05 to allow for an estimation of Fe3+

Table 2. continued

Biotite	06CH52	06CH54	07CH24	06CH45 calc.	Epidote	07CH37 core	07CH37 rim	02CH42 core	02CH42 rim	MORB calc.	MORB calc.	06CH53 rim	02CH44	02CH44 calc.
SiO_2	34.30	35.99	37.70		SiO_2	38.28	37.49	38.36	38.26			37.65	38.18	
Al_2O_3	17.23	18.21	15.08		Al_2O_3	28.12	26.60	27.96	25.27			24.60	26.63	
TiO_2	1.68	1.49	1.85		Fe_2O_3	7.71	10.32	6.78	10.32			10.49	9.74	
FeO	23.81	20.03	17.55		Mn_2O_3	0.11	0.09	0.13	0.02			0.02	0.05	
MgO	7.70	9.50	12.63		TiO_2	0.13	0.18	0.09	0.21			0.04	0.16	
MnO	0.66	0.15	0.11		MgO	0.02	0.02	0.02	0.00			0.03	0.10	
CaO	0.03	0.01	0.07		CaO	23.66	23.70	24.10	24.13			23.51	23.52	
BaO	0.09	0.08	0.11		BaO	0.00	0.00	0.02	0.00			0.00	0.08	
Na_2O	0.35	0.02	0.04		K_2O	0.00	0.00	0.00	0.01			0.01	0.02	
K_2O	9.26	8.95	9.79		Na_2O	0.03	0.00	0.00	0.03			0.01	0.02	
H_2O’	3.79	3.90	3.95	(550°C/ 6.5 kbar)	H_2O’	1.91	1.87	1.92	1.91	(350°C/ 4 kbar)	(500°C/ 7 kbar)	1.88	1.91	(600°C/ 12 kbar)
Sum	98.88	98.33	99.00		Sum	99.97	100.26	99.38	100.15			98.23	100.40	
Si	2.715	2.764	2.860	2.780	Si	3.000	3.000	3.000	3.000	3.000	3.000	3.000	3.000	3.000
Alt	1.285	1.236	1.140	1.220	Al	2.597	2.509	2.577	2.335	2.720	2.440	2.310	2.466	2.320
Sum	4.000	4.000	4.000	4.000	Ti	0.008	0.011	0.005	0.012			0.002	0.009	
Alo	0.322	0.413	0.209	0.220	Mg	0.002	0.002	0.003	0.000			0.004	0.012	
Ti	0.100	0.086	0.106		Mn	0.007	0.005	0.008	0.001			0.002	0.003	
Fe	1.576	1.286	1.113	1.670	Fe	0.455	0.622	0.399	0.609	0.280	0.560	0.629	0.576	0.680
Mg	0.909	1.087	1.429	1.080	Sum	3.068	3.149	2.992	2.957	3.000	3.000	2.946	3.066	3.000
Mn	0.044	0.010	0.007	0.030	Ca	1.986	2.032	2.019	2.027	2.000	2.000	2.008	1.980	2.000
Sum	2.950	2.882	2.864	3.000	Na	0.005	0.000	0.000	0.004			0.001	0.004	
Ca	0.003	0.000	0.005		Sum	1.991	2.032	2.019	2.031			2.009	1.984	
Ba	0.003	0.003	0.003		K	0.000	0.000	0.000	0.001			0.001	0.002	
Na	0.054	0.003	0.007		Ba	0.000	0.000	0.001	0.000			0.000	0.002	
K	0.936	0.877	0.948	1.000	OH	1.000	1.000	1.000	1.000	1.000	1.000	1.000	1.000	1.000
Sum	0.941	0.883	0.963		O’	12.093	12.261	12.009	11.971			11.928	12.083	
OH	2.000	2.000	2.000	2.000										

Proportions of cations are based on normalization of Si to 3 cations
Normalization on the basis of 11 negative charges

Table 2. continued

Chlorite	02CH37	06CH63	06CH42	MORB calc.	MORB calc.	06CH45	06CH45 calc.	CH021503	06CH57	02CH44	06CH46	06CH43	06CH40	06CH52
SiO_2	26.71	26.44	29.53			24.50		23.77	25.70	25.46	24.19	28.01	25.14	25.30
Al_2O_3	20.25	20.61	18.78			21.66		21.46	21.15	20.61	20.82	18.73	20.67	19.31
TiO_2	0.04	0.04	0.04			0.07		0.06	0.08	0.07	0.07	0.07	0.21	0.05
FeO	21.74	19.81	19.19			31.27		33.12	25.66	25.46	32.73	27.99	29.13	31.12
MgO	18.52	19.17	18.40			11.09		9.50	14.49	15.69	10.54	10.62	12.11	12.02
MnO	0.29	0.30	0.30			0.22		0.28	0.17	0.15	0.31	0.20	0.17	0.32
H_2O'	11.62	11.56	11.73	(350°C/ 4 kbar)	(350°C/ 7 kbar)	11.16	(350°C/ 7 kbar)	10.94	11.34	11.33	11.02	10.98	11.12	11.06
Sum	99.16	97.93	97.97			99.96		99.13	98.59	98.77	99.67	96.60	98.56	99.17
Si	2.756	2.756	2.756	3.000	2.950	2.632	3.000	2.632	2.632	2.632	2.632	2.632	2.632	2.632
Alt	1.244	1.244	1.244	1.000	1.050	1.368	1.000	1.368	1.368	1.368	1.368	1.368	1.368	1.368
Sum	4.000	4.000	4.000	4.000	4.000	4.000	4.000	4.000	4.000	4.000	4.000	4.000	4.000	4.000
Alo	1.218	1.264	1.281	1.000	1.100	1.373	1.000	1.379	1.355	1.265	1.303	1.473	1.338	1.210
Ti	0.003	0.003	0.003			0.005		0.005	0.006	0.005	0.006	0.006	0.017	0.004
Mn	0.026	0.027	0.026			0.020		0.026	0.016	0.013	0.029	0.019	0.015	0.029
Fe	1.877	1.719	1.641	2.000	1.240	2.809	3.250	3.037	2.269	2.254	2.979	2.558	2.627	2.821
Mg	2.848	2.966	2.804	3.000	3.660	1.777	1.750	1.553	2.285	2.475	1.709	1.567	1.947	1.943
Sum	5.971	5.978	5.754	6.000	6.000	5.985	6.000	6.000	5.931	6.012	6.026	5.622	5.945	6.007
OH	8.000	8.000	8.000	8.000	8.000	8.000	8.000	8.000	8.000	8.000	8.000	8.000	8.000	8.000

Cations based on 28 negative charges; H_2O calculated on the basis of OH = 8

Table 3. Whole-rock analyses (A) and simplified compositions used for the calculation of pseudosections (B; Figs 7–9)

	A			B		Average
	02CH44	06CH45		02CH44	06CH45	MORB*
SiO_2	53.91	59.92	SiO_2	54.79	59.96	47.73
TiO_2	1.93	1.06	TiO_2	1.94	1.06	1.24
Al_2O_3	19.26	18.71	Al_2O_3	19.58	18.72	15.46
Fe_2O_3	10.65	7.37	FeO	9.75	6.59	8.40
MgO	2.13	2.19	CaO	2.17	0.24	10.97
MnO	0.16	0.07	MgO	2.16	2.19	7.36
CaO	2.14	0.24	MnO	0.16	0.07	0.00
Na_2O	1.47	2.51	K_2O	3.60	3.95	0.09
K_2O	3.54	3.94	Na_2O	1.08	2.51	2.63
P_2O_5	0.30	0.14	H_2O	4.72	4.73	6.00
CO_2	0.16	0.51	O_2	0.04	0.00	0.12
H_2O	3.64	2.87	Sum	100.00	100.00	100.00
Sum	99.30	99.53				

*Taken from Massonne & Willner (2008)

Ar isotopes produced by the reactions on K or Ca in the samples. The Ar isotopic analytical system at Universität Potsdam consists of (1) a New Wave Gantry Dual Wave laser ablation system with a 50W CO_2 laser (wavelength 10.6 micrometres) and 6 mJ UV pulse laser (wavelength 266 nanometres, frequency-quadrupled) for heating and extracting gas from the samples, (2) an ultrahigh vacuum purification line with SAES getters and a cold trap and (3) a Micromass 5400 noble gas mass spectrometer with a high sensitivity and an ultra-low background. The mass spectrometer has adopted a pulse counting system with an electron multiplier, which effectively works for the analysis of very small amounts of gas. Fish Canyon Tuff sanidine and the K_2SO_4 and CaF_2 crystals were heated by a defocused continuous CO_2 laser beam with a similar diameter to the grain size for 1 minute. The unknown samples of the polished thick-sections were ablated by the UV pulse laser with the following conditions: 50 micrometre beam size, 2 minutes pulsing duration and 10 Hz repetition rate. The extracted gas was exposed to SAES getters and a cold trap, where the metal finger-tube was cooled down to the freezing temperature of ethanol for 10 minutes to purify the sample gas to pure Ar gas. Finally, the purified Ar gas was introduced to the noble gas mass spectrometer, Micromass 5400, to determine the Ar isotopic ratios. The Ar isotopic ratios of the sample gas were finally obtained after corrections for blank, mass discrimination by the analytical results of atmospheric argon, interference of the Ar isotopes derived from Ca and K by the irradiation, and the decay of the radiogenic Ar isotopes (^{37}Ar and ^{39}Ar) produced by the irradiation. The calculation of the ages and errors was performed according to Uto *et al.* (1997). Two approaches were used to obtain ages reflecting peak metamorphic conditions or resettings from white-mica: (a) *in situ* UV laser ablation analysis on single grains or parts of grains in a defined fabric of a polished thick-section and (b) stepwise heating analysis of a single large grain (1.5 mm) with a CO_2 laser for one very coarse-grained sample. The data are presented in Table 4. During the discussion we will show that

all ages obtained in this study are related to crystallization at temperatures below the value of ~ 350–420 °C commonly accepted as the white-mica Ar closure temperature (McDougall & Harrison, 1999 and references therein). Although Ar diffusive loss from a crystal structure is commonly assumed to be dependent on temperature and cooling rate, Villa (1998) had also argued that strain and fluid availability are more important in isotope redistribution, and also closure temperatures are higher in the case of fluid access.

Zircon crystals were separated, mounted, polished and etched according to the techniques outlined by Thomson & Ring (2006). The samples were analysed by applying the external detector method and irradiated at the Oregon State University Triga Reactor, Corvallis, USA. The neutron fluence was monitored for zircon using Corning uranium-dosed glass CN2 as well as Institute for Reference Materials and Measurements uranium-dosed glass IRMM541. Spontaneous and induced FT densities were counted using an Olympus BX51 microscope at × 1250 magnification. Central ages (Galbraith & Laslett, 1993) were calculated using the IUGS recommended zeta calibration approach of Hurford & Green (1983), which allows for non-Poissonian variation within a population of single-grain ages belonging to an individual sample. The v2 test indicates the probability that all grains counted belong to a single population of ages; a probability of less than 5 % is taken as evidence for a significant spread of single-grain ages. A spread in individual grain ages can result either from inheritance of detrital grains from mixed source areas, or from differential annealing in grains of different composition by heating within a narrow range of temperatures (Green *et al*. 1989). Zeta calibration factors of 130.7 ± 2.8 (CN2 for samples 02CHXX) and 121 ± 3.2 (IRMM541 for samples 06CHXX) were obtained by repeated calibration against a number of internationally agreed age standards according to the recommendations of Hurford (1990). Data are presented in Table 5. Fission tracks in zircon shorten or anneal with increased temperature and duration of heating. For pristine zircon grains, annealing over geological time begins at 250 ± 20 °C, with total resetting occurring above 310 ± 20 °C (Tagami *et al*. 1998), although these temperatures are lower in zircons with high accumulated radiation damage (Rahn *et al*. 2004). This translates into a closure temperature for fission tracks in zircon at moderate-to-fast cooling rates of 280 ± 30 °C, which correlates well with the brittle/ductile transition (Brix *et al*. 2002).

4. Results

4.a. Petrographical characteristics and mineral compositions

4.a.1. The Choapa Metamorphic Complex

Metamorphic banding of alternating phyllosilicate and quartz-rich laminae forming microlithons of 0.2–2 cm defines the characteristic transposition foliation of the CMC. The mineral assemblage is typically uniform and monotonous: quartz–albite–white-mica–chlorite. Locally some biotite has formed (06CH54, 07CH27) and epidote, zircon, tourmaline, titanite and ilmenite are common accessories. Quartz and albite (0.05–0.30 mm) constitute a fully recrystallized polygonal matrix between the bands of oriented phyllosilicates, which show frequent cross-cutting grains. In some samples conspicuous millimetre-sized albite porphyroblasts grew across the transposition foliation and contain crenulated graphite inclusion trails (Fig. 3a). Also, occasional small chlorite pseudomorphs (0.5 mm) after garnet occur (02CH36).

White-mica is muscovite to phengite (Si 3.09–3.29 atoms per formula unit (apfu); Fig. 4) with variable contents of Na (0.05–0.12 apfu), Ti (0.003–0.020 apfu) and X_{Mg} (0.39–0.55 in CH021503, 0.52–0.74 in 06CH63). Biotite shows an intermediate X_{Mg} (0.45–0.46) and low Ti contents (0.17–0.18 apfu). Plagioclase is mostly albite, but contains 30–41 mole % anorthite in biotite-bearing sample 06CH54. Chlorite contains 2.5–2.7 Si apfu and has an X_{Mg} of 0.32–0.41 with low contents of Mn (0.01–0.02 apfu) and Ti (0.002–0.003 apfu).

An exceptionally coarse-grained garnet mica-schist (02CH44) in the Quebrada Los Caldos (Fig. 2) is characterized by the assemblage garnet–quartz–white-mica–chlorite–epidote–rutile. Garnet porphyroblasts (1–5 mm) contain trails of titanite, rutile, ilmenite or quartz (0.01–0.05 mm), that are at an angle to the orientation of the prevailing foliation within the matrix, but also occasional inclusions of white-mica, chlorite and epidote (Fig. 3b). Garnet overgrew a polygonal fabric of coarser quartz similar to that in the surrounding matrix during a final growth stage. Garnet grains are euhedral or partly replaced by white-mica and chlorite at the rims, often also along cracks. Dominant white-mica and minor chlorite (0.2–0.5 mm) are oriented within a matrix of polygonal quartz (0.05–0.3 mm), pointing to two foliations. The phyllosilicates recrystallized in crenulation hinges and abundant white-mica grains cross-cut the crenulation cleavage. Subhedral grains of unoriented epidote (0.05–0.10 mm) are abundant in the foliation planes. Rutile occurs as rounded, unoriented crystals of 0.1–0.5 mm size in the matrix, frequently overgrown by narrow rims of retrograde titanite. Euhedral and strongly zoned tourmaline crystals are abundant in the matrix.

White-mica in garnet mica-schist (02CH44) is mostly phengite (3.10–3.26 Si apfu; Fig. 4) with enhanced Na (0.04–0.16 apfu) and Ti (0.01–0.03 apfu) and variable, but intermediate X_{Mg} (0.31–0.57). Si contents decrease from core to rim. Chlorite shows Si contents of 2.7–3.2 apfu and an X_{Mg} of 0.26–0.34. Epidote contains 0.55–0.68 Fe apfu. Garnet composition is $almandine_{0.60–0.71}$, $grossular_{0.15–0.22}$, $pyrope_{0.05–0.18}$, $spessartine_{0.01–0.10}$, $andradite_{0.00–0.04}$. From core to rim, pyrope and almandine components as well as X_{Mg} increase, whereas grossular and spessartine components decrease.

Greenschists of the CMC contain Ca-amphibole, chlorite, quartz and plagioclase–epidote–rutile±

Table 4. $^{40}Ar/^{39}Ar$ isotopic ratios and ages of single white-mica grains measured by UV laser ablation

Sample Name	Lab-ID	Age	±1σ	$^{40}Ar^{*}/^{39}Ar_K$	±1σ	$^{40}Ar/^{39}Ar$	±1σ	$^{37}Ar/^{39}Ar$	±1σ	$^{36}Ar/^{39}Ar$ ($\times10^{-3}$)	±1σ	$^{40}Ar^{*}$ (%)	K/Ca	$^{39}Ar_K$ %		
02CH44	U07006	197.82	5.55	68.86	2.02	206.64	1.89	0.463	0.03	466.6	7.3	33.3	1.27			
(spot age dating)		203.99	7.66	71.13	2.81	334.65	3.92	0.290	0.03	892.0	13.7	21.2	2.03			
		244.79	3.12	86.35	1.12	139.08	1.11	0.171	0.01	178.6	3.1	62.1	3.45			
J:0.001683		273.60	2.19	97.30	0.75	108.95	0.52	0.051	0.01	39.4	2.0	89.3	11.59			
Garnet		274.63	2.21	97.70	0.75	118.47	0.56	0.046	0.01	70.3	2.0	82.5	12.84			
mica-schist		277.45	2.34	98.78	0.81	123.72	0.68	0.213	0.01	84.6	1.9	79.8	2.76			
Choapa		278.09	1.72	99.02	0.53	121.72	0.41	0.047	0.01	76.8	1.4	81.4	12.43			
Complex		282.22	1.90	100.62	0.61	107.43	0.41	0.006	0.01	23.1	1.6	93.7	103.25			
		283.86	1.69	101.25	0.51	111.79	0.41	0.002	0.00	35.7	1.2	90.6	315.67			
		293.88	2.54	105.12	0.89	153.75	0.37	0.003	0.01	164.6	2.9	68.4	201.27			
		294.85	2.51	105.50	0.88	132.63	0.87	0.001	0.01	91.8	1.9	79.5	477.69			
		297.34	2.26	106.46	0.77	123.16	0.66	0.004	0.01	56.5	1.8	86.4	134.63			
		306.75	2.63	110.12	0.93	200.92	1.12	0.452	0.47	307.6	2.8	54.8	1.30			
02CH44	C09019	273.89	11.78	95.87	4.43	132.12	0.60	0.274	27.43	122.9	1.4	72.5	2.14	5.80		
(stepwise heating)		296.78	3.79	104.57	1.39	106.48	0.30	0.082	8.18	6.5	0.3	98.2	7.19	19.46		
		304.19	3.70	107.40	1.35	108.47	0.52	0.075	7.49	3.7	0.3	99.0	7.86	21.29		
J:0.001710		302.93	3.18	106.92	1.14	107.75	0.38	0.065	6.45	2.9	0.4	99.2	9.12	24.74		
		305.69	2.87	107.98	1.01	109.48	0.41	0.056	5.56	5.1	0.2	98.6	10.57	28.70		
		302.92	*1.66*	*(Plateau age)*		(steps 2–5)										
		301.10	*1.92*	*(Total gas age)*												
06CH45	U07007	241.60	12.21	85.14	4.59	162.75	2.88	0.010	0.086	262.6	15.3	52.3	57.38			
(spot age dating)		247.96	2.77	87.54	0.99	146.88	0.71	0.025	0.010	200.8	3.2	59.6	23.11			
		251.61	3.18	88.93	1.15	137.40	1.12	0.003	0.018	164.0	3.3	64.7	216.55			
J:0.001683		263.08	1.76	93.28	0.56	104.74	0.54	0.001	0.004	38.8	1.0	89.1	515.78			
Phyllite		267.11	1.86	94.82	0.60	101.26	0.41	0.018	0.009	21.8	1.6	93.6	32.37			
Choapa		270.61	2.51	96.16	0.88	126.83	0.52	0.028	0.012	103.8	2.7	75.8	21.02			
Complex		271.80	1.78	96.61	0.56	109.61	0.36	0.002	0.008	44.0	1.6	88.1	342.68			
		272.78	1.72	96.99	0.53	103.68	0.46	0.006	0.006	22.6	1.1	93.5	101.21			
		275.45	7.22	98.01	2.74	141.00	2.14	0.006	0.035	145.5	8.1	69.5	103.00			
		278.64	3.38	99.24	1.24	172.01	1.38	0.016	0.014	246.3	3.7	57.7	36.15			
02CH42	U07010	187.94	3.17	64.66	1.12	144.24	1.29	0.422	0.024	269.6	3.9	44.8	1.39			
(spot age dating)		188.78	3.94	64.96	1.41	140.15	1.02	0.591	0.021	254.8	4.7	46.3	0.99			
		188.27	*2.47*	*(Weighted average)*												
J:0.001698		197.67	8.51	68.20	3.09	263.90	3.88	2.089	0.060	663.7	13.8	25.8	0.28		normal isochron age:	212 ± 5 Ma
Greenschist		203.99	3.63	70.50	1.29	173.32	1.42	0.528	0.030	348.3	4.2	40.7	1.11		MSWD	1.67
Choapa		211.07	3.96	73.10	1.42	110.21	1.00	0.309	0.025	125.8	4.4	66.3	1.91		initial $^{40}Ar/^{36}Ar$ ratio:	293 ± 5
Complex		217.09	4.93	75.31	1.79	174.96	1.63	0.357	0.027	337.5	6.3	43.0	1.65		inverse isochron age:	212 ± 5 Ma
		226.55	11.56	78.80	4.27	189.25	1.75	6.475	0.134	378.3	14.5	41.4	0.09		MSWD	1.70
		227.19	11.04	79.04	4.07	245.77	5.62	4.342	0.150	567.3	17.6	32.0	0.13		initial $^{40}Ar/^{36}Ar$ ratio:	293 ± 5
		209.98	*2.18*	*(Weighted average)*												

Table 4. continued

Sample Name	Lab-ID	Age	±1σ	$^{40}Ar^*/^{39}Ar_K$	±1σ	$^{40}Ar/^{39}Ar$	±1σ	$^{37}Ar/^{39}Ar$	±1σ	$^{36}Ar/^{39}Ar$ ($\times10^{-3}$)	±1σ	$^{40}Ar^*$ (%)	K/Ca		$^{39}Ar_K$ %	
06CH63 (spot age dating)	U07008	135.61	4.38	46.77	1.56	71.74	1.09	1.193	0.035	85.2	4.8	65.1	0.49			
		161.82	6.11	56.23	2.21	82.93	0.96	2.960	0.065	92.2	7.2	67.6	0.20		normal isochron age:	168 ± 5 Ma
J:0.001669		165.83	5.80	57.68	2.10	68.30	0.85	1.230	0.043	36.7	6.7	84.4	0.48		MSWD	1.02
Greenschist		166.47	9.36	57.92	3.40	101.63	1.85	4.088	0.118	150.5	11.2	56.8	0.14		initial $^{40}Ar/^{36}Ar$ ratio:	297 ± 20
Choapa		167.26	8.99	58.21	3.27	105.15	1.68	3.407	0.102	161.0	10.8	55.2	0.17		inverse isochron age:	168 ± 5 Ma
Complex		173.28	4.22	60.40	1.52	70.72	0.60	1.013	0.046	35.6	4.8	85.3	0.58		MSWD	1.06
		181.20	9.58	63.30	3.51	109.90	1.37	1.924	0.068	158.9	11.7	57.5	0.31		initial $^{40}Ar/^{36}Ar$ ratio:	298 ± 19
		169.25	*2.60*	*(Weighted average)*												
06CH54	U07009	127.37	1.44	43.83	0.48	76.18	0.24	1.182	0.046	110.2	1.6	57.5	0.50			
(spot age dating)		130.32	1.42	44.88	0.47	71.53	0.48	0.061	0.011	90.2	1.4	62.7	9.64			
		133.79	1.57	46.12	0.53	63.29	0.39	0.072	0.006	58.1	1.6	72.9	8.21			
J:0.001669		136.00	1.21	46.91	0.39	59.50	0.33	0.115	0.010	42.7	1.0	78.8	5.11			
Phyllite		137.28	1.09	47.37	0.34	57.34	0.21	0.030	0.006	33.8	1.0	82.6	19.81			
Choapa		137.69	1.99	47.52	0.69	60.78	0.60	0.052	0.007	44.9	1.7	78.2	11.41			
Complex		141.64	1.72	48.94	0.59	53.02	0.50	0.027	0.006	13.8	1.2	92.3	21.79			
		142.51	1.11	49.25	0.35	52.53	0.15	0.007	0.005	11.1	1.1	93.7	78.93			
06CH43	U08017	227.42	4.34	66.14	1.32	84.05	1.06	0.023	0.001	60.6	3.5	78.7	26.06			
(spot age dating)		235.02	5.63	68.50	1.73	91.39	1.33	0.039	0.001	77.5	4.9	75.0	15.21			
		237.93	6.01	69.41	1.85	92.76	0.70	0.063	0.003	79.1	6.0	74.8	9.40			
J:0.002031		240.95	2.71	70.35	0.80	88.15	0.63	0.003	0.000	60.2	2.0	79.8	206.58			
Metagreywacke		242.97	5.42	70.98	1.67	91.23	1.26	0.055	0.001	68.5	4.6	77.8	10.77			
Arrayán		251.15	5.80	73.54	1.80	94.20	0.97	0.011	0.001	69.9	5.5	78.1	51.33			
Formation		251.49	5.37	73.64	1.66	96.17	1.22	0.049	0.002	76.2	4.7	76.6	12.07			
02CH43	U08020	207.10	14.96	59.85	4.57	172.35	5.57	0.113	0.268	380.8	18.6	34.7	5.20			
(spot age dating)		207.22	29.64	59.88	9.07	233.46	6.01	2.201	0.584	588.7	33.4	25.6	0.27			
		207.32	8.71	59.92	2.65	93.78	0.98	0.944	0.181	115.2	8.7	63.8	0.62			
		207.31	*7.30*	*(Weighted average)*												
J:0.002033		224.10	10.28	65.07	3.16	129.58	1.65	0.115	0.137	218.4	10.7	50.2	5.09		normal isochron age:	251 ± 8 Ma
Metagreywacke		240.88	15.55	70.28	4.84	150.36	1.82	0.146	0.234	271.1	16.4	46.7	4.04		MSWD	1.40
Arrayán		241.59	6.44	70.50	1.99	99.56	0.52	0.108	0.071	98.4	6.6	70.8	5.46		initial $^{40}Ar/^{36}Ar$ ratio:	276 ± 15
Formation		247.02	11.25	72.20	3.51	150.58	1.29	0.036	0.251	265.3	11.8	47.9	16.20		inverse isochron age:	253 ± 7 Ma
		257.33	6.96	75.43	2.17	93.84	1.57	0.165	0.112	62.4	6.0	80.4	3.56		MSWD	1.41
		244.64	*3.89*	*(Weighted average)*											initial $^{40}Ar/^{36}Ar$ ratio:	275 ± 14
06CH40	U08016	179.84	11.68	51.59	3.51	80.86	1.80	0.016	0.180	99.1	11.3	63.8	36.00	*	normal isochron age:	200 ± 6 Ma
(spot age dating)		190.51	4.49	54.81	1.34	84.30	0.55	0.121	0.086	99.8	4.3	65.0	4.87		MSWD	1.68
		200.03	6.39	57.71	1.93	109.45	0.74	0.106	0.115	175.2	6.3	52.7	5.56		initial $^{40}Ar/^{36}Ar$ ratio:	287 ± 19
J:0.002032		201.88	5.75	58.27	1.74	73.93	0.70	0.134	0.114	53.1	5.6	78.8	4.38	*	inverse isochron age:	203 ± 6 Ma
Metagreywacke		204.77	4.71	59.15	1.42	79.01	0.39	0.027	0.132	67.2	4.7	74.9	21.56		MSWD	1.73
Arrayán		208.50	6.65	60.29	2.02	76.40	1.39	0.125	0.149	54.6	5.8	78.9	4.69	*	initial $^{40}Ar/^{36}Ar$ ratio:	287 ± 18
Formation		224.75	11.30	65.29	3.48	90.77	1.14	0.142	0.108	86.3	11.4	71.9	4.15		*detrital	
		200.21	*2.31*	*(Weighted average)*												
		240.77	5.50	70.26	1.69	92.52	1.39	0.050	0.119	75.3	4.6	75.9	11.71			

Table 4. continued

Sample Name	Lab-ID	Age	±1σ	$^{40}Ar^*/^{39}Ar_K$	±1σ	$^{40}Ar/^{39}Ar$	±1σ	$^{37}Ar/^{39}Ar$	±1σ	$^{36}Ar/^{39}Ar$ ($\times10^{-3}$)	±1σ	$^{40}Ar^*$ (%)	K/Ca		$^{39}Ar_K$ %		
06CH46 (spot age dating)	U08018	136.36	7.10	38.68	2.08	128.32	0.87	0.037	0.042	303.4	7.0	30.1	15.81			normal isochron age:	181 ± 5 Ma
		164.81	3.55	47.12	1.05	85.31	0.83	0.017	0.038	129.2	3.0	55.2	35.40	*		MSWD	0.31
J:0.002030		169.66	4.20	48.57	1.24	75.08	0.47	0.028	0.053	89.7	4.1	64.7	21.33	*		initial $^{40}Ar/^{36}Ar$ ratio:	257 ± 17
Metagreywacke		172.97	3.06	49.57	0.90	71.69	0.66	0.015	0.014	74.9	2.5	69.1	39.19	*		inverse isochron age:	181 ± 5 Ma
Arrayán		173.70	2.83	49.78	0.83	66.54	0.73	0.019	0.029	56.7	1.9	74.8	30.74	*		MSWD	0.31
Formation		*170.94*	*1.65*	*(Weighted average)*												initial $^{40}Ar/^{36}Ar$ ratio:	257 ± 17
																*crystallized in fissure	
		185.52	4.13	53.35	1.23	97.51	1.16	0.097	0.054	149.5	3.4	54.7	6.06				
		189.07	5.49	54.43	1.65	98.84	1.60	0.023	0.047	150.3	4.7	55.1	25.20				
		201.04	2.68	58.07	0.78	83.47	0.89	0.028	0.028	86.0	1.6	69.6	21.24				
02CH62	U08021	155.89	2.57	44.56	0.75	63.60	0.62	0.056	0.025	64.5	2.1	70.1	10.42			normal isochron age:	166 ± 6 Ma
(spot age dating)		156.85	2.37	44.85	0.68	60.47	0.74	0.031	0.043	52.9	1.5	74.2	18.73			MSWD	0.94
		158.20	1.61	45.25	0.44	61.33	0.21	0.043	0.025	54.4	1.4	73.8	13.82			initial $^{40}Ar/^{36}Ar$ ratio:	255 ± 32
J:0.002025		159.80	2.02	45.73	0.58	61.34	0.33	0.018	0.019	52.8	1.7	74.6	33.07			inverse isochron age:	167 ± 6 Ma
Metapelite		160.74	2.51	46.01	0.73	63.14	0.45	0.025	0.029	58.0	2.2	72.9	23.56			MSWD	0.94
Huentelauquén		160.90	2.04	46.06	0.58	57.97	0.31	0.022	0.022	40.3	1.8	79.5	27.21			initial $^{40}Ar/^{36}Ar$ ratio:	250 ± 32
Formation		161.22	1.69	46.16	0.47	60.98	0.21	0.003	0.011	50.2	1.5	75.7	203.03				
		159.30	*0.76*	*(Weighted average)*													
06CH52	U08019	101.21	29.78	28.44	8.61	434.00	8.48	0.036	0.298	1372.5	39.0	6.6	16.16	*		* detrital	
(spot age dating)		113.06	42.32	31.88	12.31	2957.40	26.41	0.114	0.108	9900.1	97.3	1.1	5.18	*			
		128.01	2.38	36.25	0.68	60.66	0.56	0.115	0.046	82.7	2.0	59.7	5.09	*			
J:0.002029		135.24	10.71	38.37	3.15	353.43	3.43	0.015	0.078	1066.2	14.4	10.9	39.25	*			
		139.81	2.73	39.72	0.79	62.78	0.56	2.565	0.125	79.4	2.4	63.1	0.23	*			
Metaconglomerate		153.84	2.36	43.88	0.68	115.43	0.64	0.014	0.027	242.2	2.4	38.0	42.58	*			
Huentelauquén		154.47	10.39	44.06	3.09	153.91	1.46	0.123	0.139	371.8	10.8	28.6	4.78	*			
Formation		164.69	2.85	47.11	0.83	98.65	0.30	0.017	0.057	174.4	2.8	47.8	35.55	*			
		175.21	9.46	50.27	2.84	74.54	0.86	0.111	0.234	82.2	9.4	67.4	5.32	*			

Table 5. Fission-track data for zircon from the metamorphic basement (31–32° S)

Sample	N	Ps (Ns)	Track density ($\times$ 106 tr cm^{-2}) Pi (Ni)	Pd (Nd)	Age Dispersion (Pχ^2)	Central age (Ma) ($\pm$ 1σ)	Unit
06CH40	12	12.28 (1096)	1.501 (134)	0.5116 (3193)	<0.01% (99 %)	249.7 ± 24.2	AF
06CH45	6	24.03 (825)	2.942 (101)	0.5093 (3179)	<0.01% (97 %)	248.3 ± 27.3	CMC
02CH49	20	18.77 (3233)	2.073 (357)	0.5070 (3164)	0.01% (97 %)	273.5 ± 17.6	AF
06CH54	1	22.34 (488)	2.472 (54)	0.5046 (3149)	n/a	271.7 ± 39.9	CMC
02CH43	10	15.05 (1455)	3.734 ‘(361)	0.4202 (5803)	5.15% (99.9 %)	109.7 ± 7.0	AF
02CH39	17	10.45 (2337)	2.968 (664)	0.4222 (5831)	4.49% (74.3 %)	96.1 ± 5.0	AF
02CH41	17	9.69 (2516)	2.538 (659)	0.4212 (5817)	0.00% (98.4 %)	104.2 ± 5.3	AF

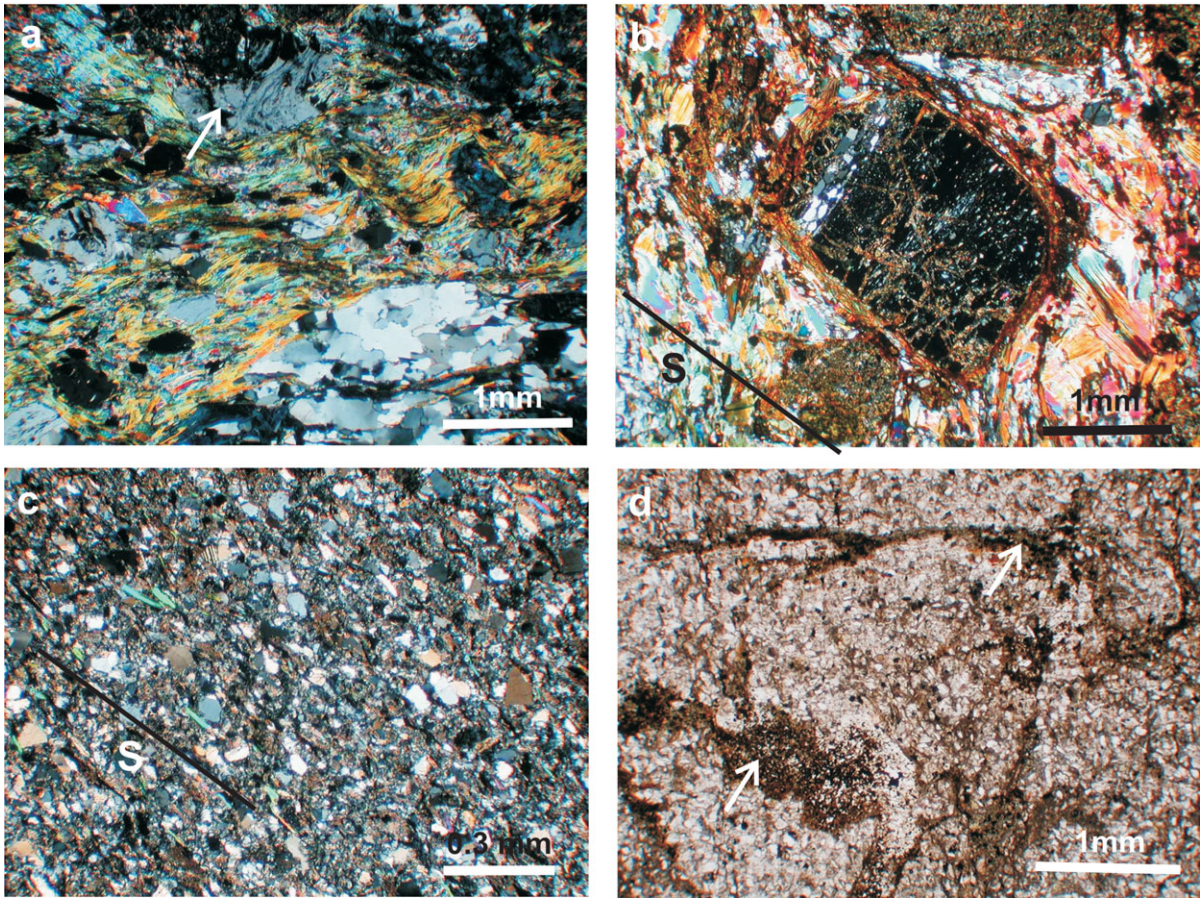

Figure 3. (Colour online) Micrographs: (a) recrystallized fabric of quartz and white-mica with albite porphyroblast (arrow) including helicitic graphite trails (phyllite 02CH45; CMC; crossed polars). (b) Garnet porphyroblast with quartz inclusion trails perpendicular to the main foliation S (black bar); rims are replaced by chlorite and white-mica (coarse-grained garnet mica-schist 02CH44; CMC; crossed polars). (c) Detrital fabric in metagreywacke 06CH40 (AF); weakly recrystallized matrix between quartz clasts; detrital white-mica oriented parallel to main foliation S (black bar; crossed polars). (d) Metagreywacke 06CH46 (AF) cataclastically deformed; fissures are filled with quartz, white-mica and haematite (plane polarized light).

white-mica (assemblage 1; samples 02CH42, 06CH55, 06CH63, 07CH23) or albite–epidote–titanite (assemblage 2; sample 02CH37) or biotite–albite–titanite (assemblage 3; sample 07CH24). Chlorite, epidote and up to 2 mm long needles of amphibole are oriented parallel to the penetrative foliation. Some grains are cross-cutting. Also, crenulations with recrystallized hinges occur. Albite porphyroblasts, biotite and white-mica grains appear occasionally. Quartz and plagioclase form small recrystallized aggregates in the nematoblastic fabric. K-feldspar is present in sample 06CH63. Retrograde titanite generally overgrew rutile. Paragonite and potassic white-mica occur in sample 02CH42.

The amphibole in rocks with assemblage 1 is strongly, but irregularly zoned (Fig. 5). The cores are usually actinolite or actinolitic hornblende with somewhat elevated Na^B contents (0.06–0.38 apfu) and uniform X_{Mg} (0.70–0.78, but 0.62–0.68 in 07CH37). Only sample 06CH63 has no actinolitic core. The rims are generally magnesiohornblende, tschermakitic hornblende to tschermakite slightly straddling the fields of pargasitic and edenitic hornblende ($(Na + K)^A$ 0.1–0.52 apfu; Na^B 0.04–0.52 apfu; nomenclature after

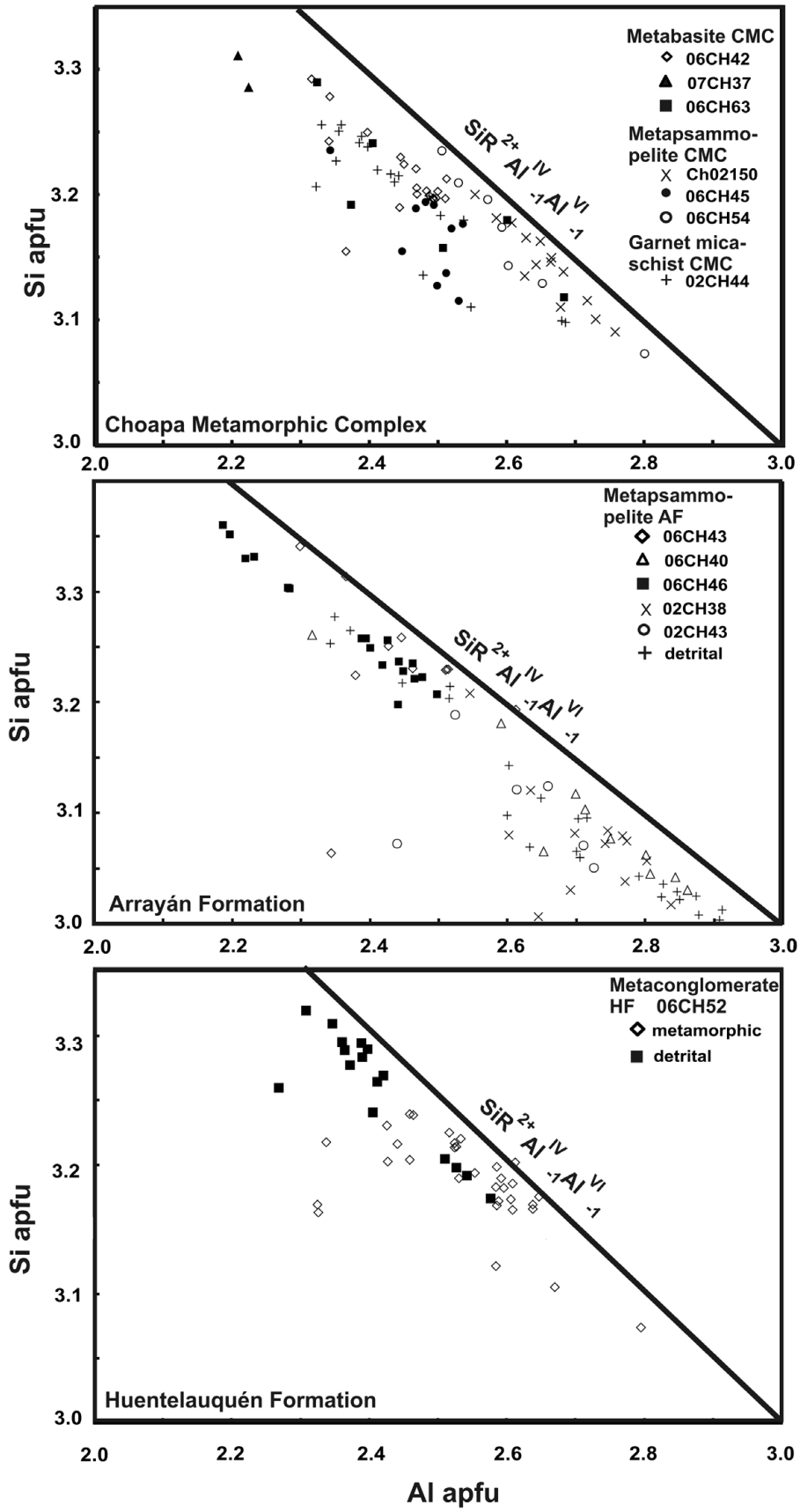

Figure 4. Si–Al variation diagram of white-mica within all studied rock types. The line of the ideal Tschermak substitution is inserted.

Leake *et al*. 1997). Their X_{Mg} is always lower than that of the corresponding core compositions (0.55–0.71). In metabasite samples 07CH24 and 07CH37, amphibole is actinolite only.

Potassic white-mica in the greenschist contains the highest Si contents (3.15–3.31 apfu) of all rock types (Fig. 4), with rather variable contents of Na (0.02–0.13 apfu), Ba (0.002–0.027 apfu), Ti (0.003–0.025

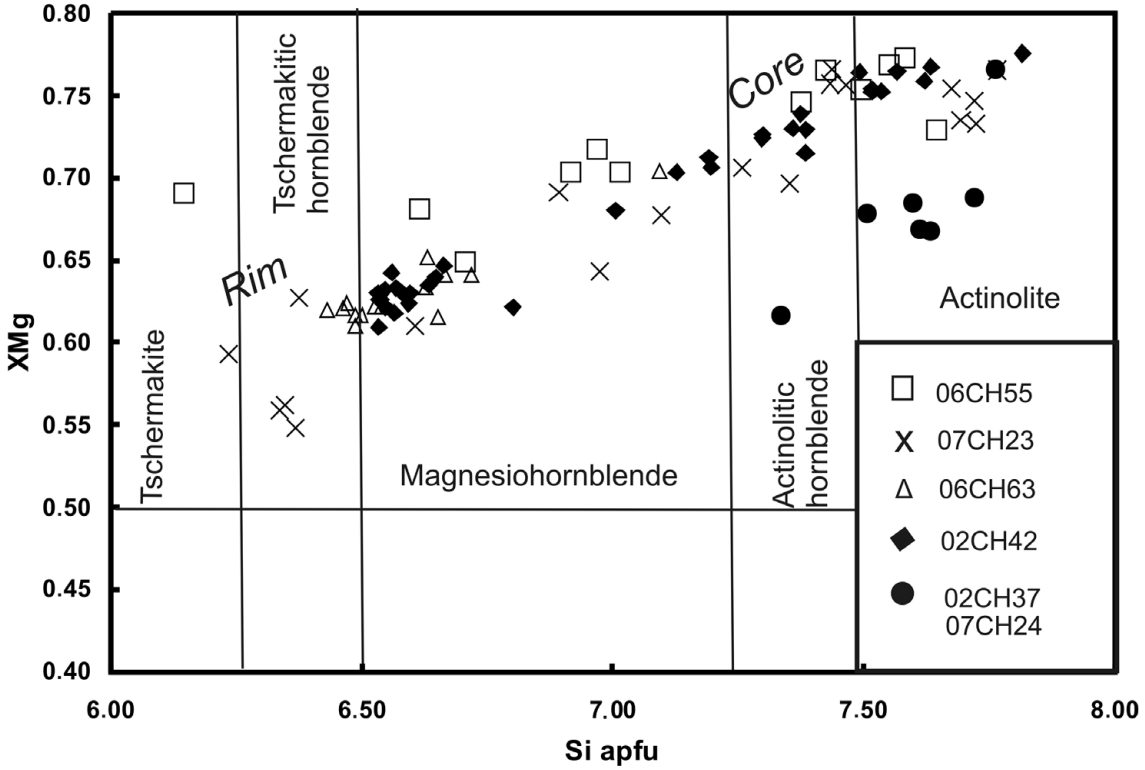

Figure 5. X_{Mg}–Si variation diagram of amphibole in metabasite samples of the CMC.

apfu) and X_{Mg} (0.65–0.8 in 02CH42, 0.48–0.97 in 06CH63). Si contents systematically decrease from core to rim. In sample 02CH42, paragonite (0.67–0.78 Na apfu) coexists with potassic white-mica. Biotite shows an intermediate X_{Mg} (0.56–0.61) and low Ti contents (0.07–0.10 apfu). Plagioclase is albite, but up to 36–38 mole % anorthite component was determined in plagioclase rims of samples 06CH55 and 07CH23. In the latter sample, albite and andesine can be regarded as first generation and second generation, respectively. Epidote occurs in two generations: the dominant one contains 0.36–0.57 Fe apfu, and an earlier generation (inclusions and core composition) 0.60–0.75 Fe apfu. Chlorite compositions are characterized by 2.6–3.0 Si apfu, X_{Mg} 0.62–0.70, 0.01–0.04 Mn apfu and 0.002–0.015 Ti apfu.

4.a.2. The Arrayán Formation

Whereas the metapelite of the AF is characterized by a penetrative cleavage, the metagreywacke shows an incipient metamorphic banding by the occasional concentration of oriented white-mica. In contrast to the metagreywacke of the CMC, the metagreywacke of the AF consistently shows a preserved fine- to coarse-grained detrital fabric with quartz, potassic feldspar, albite, white-mica and chlorite as mineral clasts (Fig. 3c). Angular lithoclasts (up to 2 mm size in coarse-grained samples) of shale, siltstone, chert, rhyolite and graphic quartz–feldspar intergrowths occur. Tourmaline, zircon, apatite, ilmenite and occasional rutile and epidote are the components of the heavy mineral spectrum. Quartz in the matrix between the clasts is variably but mostly weakly recrystallized. The preserved quartz clasts are embedded in a fine-grained recrystallized matrix with a grain size of 0.01–0.02 mm. Metamorphic white-mica and chlorite (0.01–0.03 mm), being significantly smaller than their detrital equivalents (0.5–2 mm), crystallized parallel to the incipient banding, whereas biotite frequently grew late at the expense of chlorite and K-feldspar in many samples. Detrital white-mica is generally strongly bent. Some quartz and albite clasts between oriented phyllosilicates are elongated with concave boundaries indicative of pressure solution. Strain-induced grain boundary migration frequently occurs at some grain contacts, particularly in some cross-cutting quartz-filled fissures. Rocks deformed to cataclasites within strike-slip zones (Fig. 2; 06CH46) are characterized by a net of fissures of variable thickness filled with very fine-grained recrystallized quartz and white-mica (Fig. 3d). These fillings are strongly stained by haematite.

A compositional variation between detrital ($>$ 50 μm grain size) and metamorphic white-mica ($<$ 20 μm grain size; Fig. 4) is not conspicuous, in contrast to observations made in very-low grade metagreywackes in the Chilean Chonos Archipelago (Willner, Hervé & Massonne, 2000). Metamorphic white-mica contains 3.01–3.36 Si apfu (Fig. 4), 0.04–0.12 Na apfu, 0.002–0.013 Ba apfu, 0.001–0.038 Ti apfu (occasional 0.06) and variable X_{Mg} (0.37–0.78 in 06CH43, 0.51–0.64 in 06CH40), whereas detrital white-mica contains 3.01–3.27 Si apfu, 0.01–0.24 Na apfu, 0.001–0.016 Ba apfu, 0.01–0.038 Ti apfu (occasional 0.07) and shows X_{Mg} values between 0.64

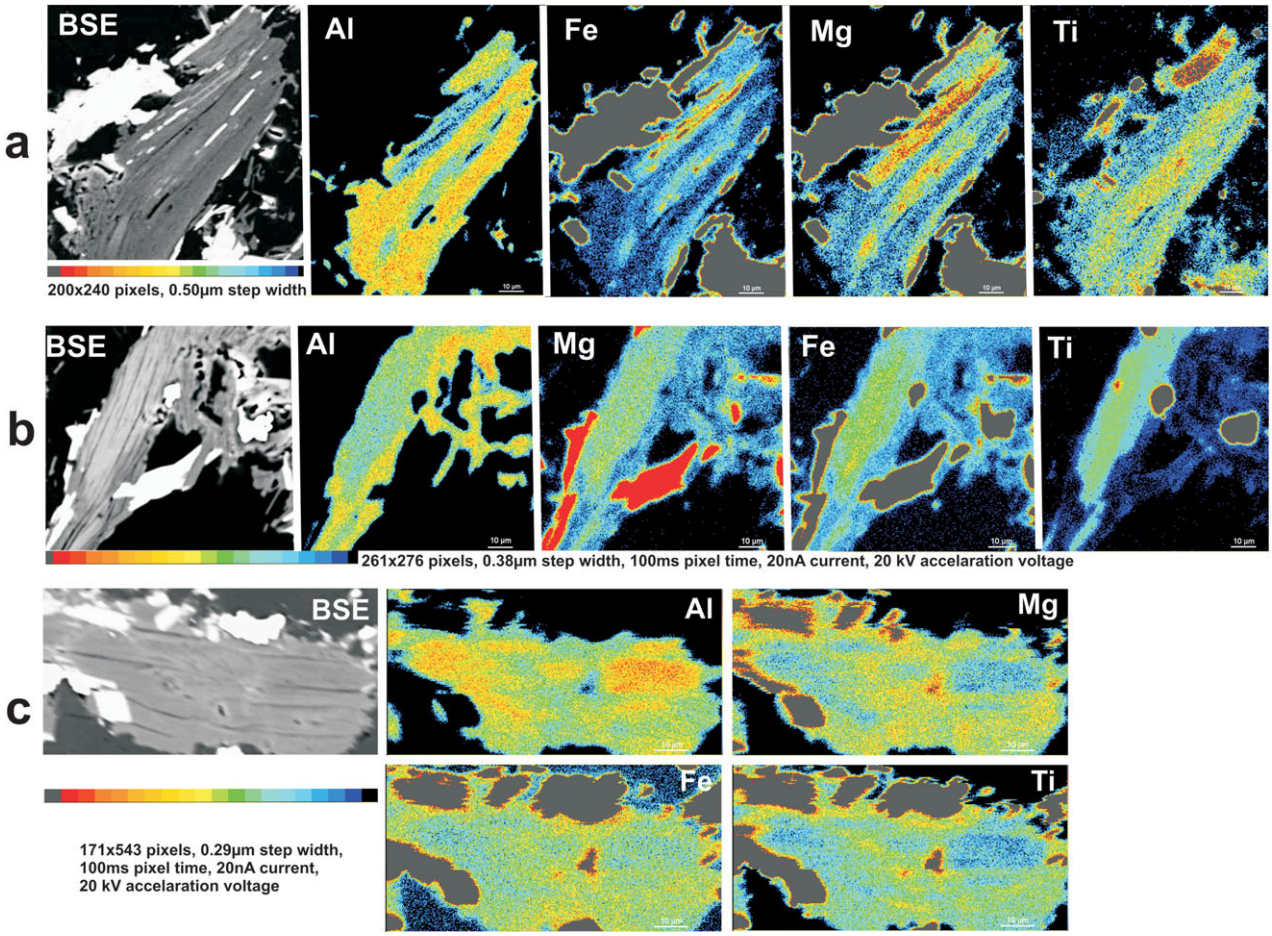

Figure 6. (Colour online) Back-scattered electron images and maps of X-ray intensity distribution of Al, Fe, Mg, and Ti in detrital white-mica from metagreywacke 06CH40 (AF; a and b) and metaconglomerate 06CH52 (HF; c). Relative intensities increase from blue to red.

and 0.90. Plagioclase is invariably albite. Chlorite has remarkably uniform Si contents of 2.6–2.9 apfu, with additional generations in sample 06CH43 (3.0–3.5 Si apfu) and samples 06CH40 and 02CH43 (2.4 Si apfu). X_{Mg} varies according to the whole-rock composition, but within a narrow range (e.g. 0.29–0.38 in samples 02CH38 and 06CH46; 0.40–0.44 in samples 06CH40). Contents of Mn (0.04–0.06 apfu) and Ti (0.002–0.011 apfu) are low in chlorite.

We studied the compositional zonation of detrital white-mica in detail by element distribution maps (Fig. 6) for later interpretation of Ar–Ar ages. Instead of a concentric growth zonation pattern, essentially two types of compositional heterogeneity became apparent: zones of lower Al (and Na) and conversely higher Si, Mg, Fe and Ti content. These zones exist (1) at the rims of large detrital white-mica (Fig. 6a) and (2) parallel to the (001) cleavage plane leaving only narrow relict zones of high-Si white-mica (Fig. 6b). Zones within the grains may also be patchy (Fig. 6c).

4.a.3. Huentelauquén Formation

The clastic metasedimentary rocks of the HF have comparable characteristics to those of the AF: the detrital fabric is still preserved and biotite is an occasional metamorphic phase in metagreywackes as well as pebbles of rhyolite and granite. The pebbles of the conspicuous conglomerate (06CH52) comprise rhyolite, granite, vein quartz, shale, sandstone and phyllite.

In the HF conglomerate, metamorphic and detrital white-mica can be identified unequivocally. Metamorphic fine-grained white-micas occurs in rhyolite and granite pebbles and shows Si contents of 3.15–3.24 apfu (Fig. 4), 0.01–0.04 Na apfu, 0.001–0.012 Ba apfu, 0.00–0.04 Ti apfu (occasionally 0.22 apfu) and X_{Mg} 0.51–0.69 and 0.34–0.46, respectively, depending on the pebble composition. Composition of detrital, oriented and large white-mica grains in phyllite clasts varies considerably among grains, but also within grains: 3.17–3.32 Si apfu, 0.01–0.08 Na apfu, 0.000–0.008 Ba apfu, 0.01–0.02 Ti apfu and X_{Mg} 0.39–0.56. It is remarkable that Na contents in metamorphic and detrital white-mica are apparently similar and uniform.

Biotite in the rhyolite pebbles is ferruginous (X_{Mg} 0.37) and has low Ti content (0.10 apfu). Chlorite is ferruginous (X_{Mg} 0.38–0.41), with Si contents similar to those in chlorite in the AF (5.3–5.5 apfu).

4.b. Pressure–temperature constraints

For an estimation of the variation of maximum *P–T* conditions within the studied rock types we used two methods:

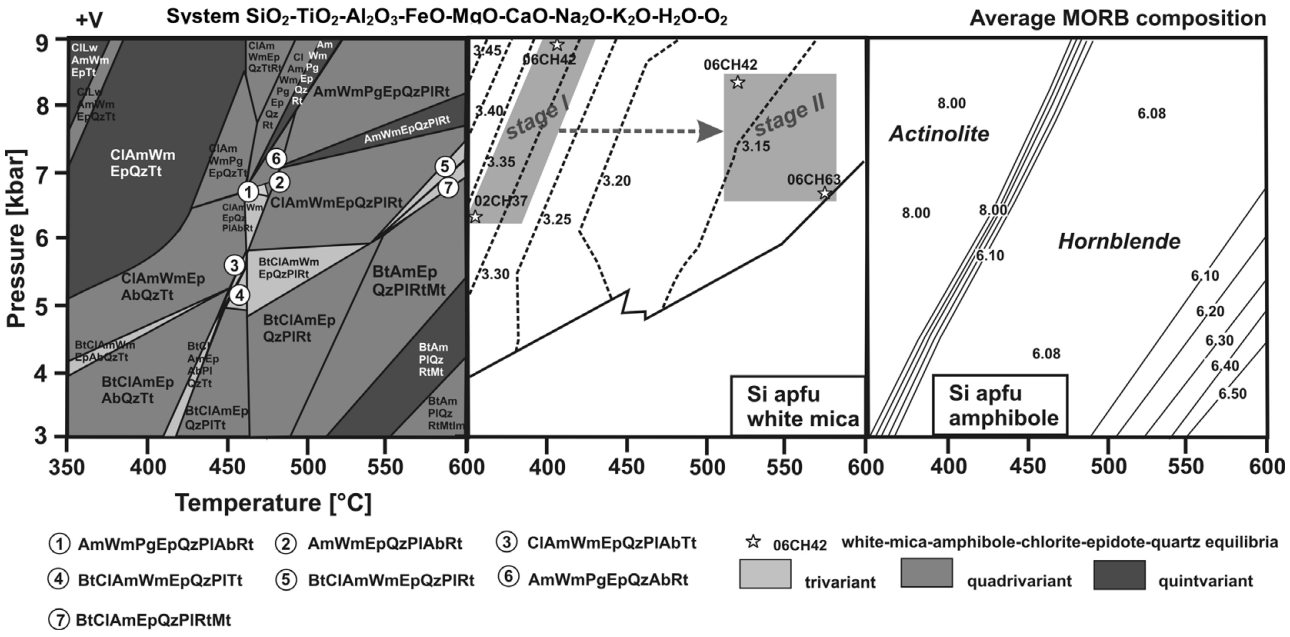

Figure 7. *P–T* pseudosection calculated for typical MORB composition (Table 3) with isolines for Si contents in white-mica and amphibole. Calculated equilibria for two stages are inserted.

Method 1: We calculated three *P–T* pseudosections for characteristic whole-rock compositions in the systems SiO_2–TiO_2–Al_2O_3–FeO–MgO–CaO–Na_2O–K_2O–H_2O–O_2 and SiO_2–TiO_2–Al_2O_3–FeO–MgO–MnO–CaO–Na_2O–K_2O–H_2O within the expected *P–T* range with the PERPLE_X software package (Connolly 1990, 2005; used version of August 2006 downloaded from http://www.perplex.ethz.ch). The thermodynamic data set of Holland & Powell (1998, updated 2002) for minerals and aqueous fluid was used. Calculations were performed using the following solid-solution models: Holland & Powell (2003) and Powell & Holland (1999) for white-mica, epidote, garnet, plagioclase, chlorite and biotite, and Dale *et al*. (2005) for amphibole. These were selected from the distributed version of the PERPLE_X solution model file. Albite, K-feldspar, quartz, titanite, H_2O and paragonite were considered as pure phases. Calculated compositions of minerals provide excellent coincidence with measured ones (Table 2), except for actinolite, where a too high Na content is calculated owing to the solid-solution model chosen.

Method 2: We also calculated multivariant reactions using the Ge0-Calc software of Brown, Berman & Perkins (1989) and derivations (TWQ) with the thermodynamic dataset of Berman (1988) augmented by compatible thermodynamic data for the end-members glaucophane from Evans (1990), clinochlore, Mg-Al-celadonite and Fe-Al-celadonite from Massonne (1995*a*) and daphnite and muscovite from Massonne & Szpurka (1997). The activity formulations used for non-ideal solid solutions of chlorite and amphibole were those by Massonne (1995*a,b*), for white-mica, those by Massonne (1995*a*, 1997), and for garnet, the one by Berman (1990), whereas an ideal solution model was chosen for epidote ($a_{clinozoisite} = 1 - X_{pistacite}$). We preferred these data instead of those by Holland & Powell (1998) used for the calculation of *P–T* pseudosections (see above) in order to get independent information on the maximum *P–T* conditions recorded. We have widely and successfully applied this approach to other low and medium grade rocks of the Chilean accretionary systems (e.g. Willner, 2005; Willner, Hervé & Massonne, 2000; Willner *et al*. 2004*a*). Hence, a better basis for comparison among the various Chilean accretionary complexes is given.

4.b.1. The Choapa Metamorphic Complex

The best *P–T* constraints for the CMC are provided by the metabasite assemblages. A *P–T* pseudosection for a typical mid-ocean ridge basalt (MORB) composition (Massonne & Willner 2008) with H_2O in excess was calculated to demonstrate the heterogeneous *P–T* evolution in the CMC metabasite (method 1; Fig. 7). In contrast to Massonne & Willner (2008), the pseudosection was calculated for a higher temperature and with a solid-solution model for amphibole that incorporates the tschermakite and edenite components (see method 1). The assemblage actinolite–biotite–chlorite–quartz–albite–titanite (07CH24; Fig. 1b) equilibrated at maximum *P–T* conditions of 4.0–4.5 kbar, 350–380 °C, constrained by the appearance of biotite instead of potassic white-mica in the presence of actinolite. The temperature for the assemblage actinolite–white-mica–chlorite–epidote–quartz–albite–titanite (02CH37) can be constrained by the position of the relevant Si isopleth for potassic white-mica (3.28–3.31 apfu) at about 350–450 °C. However, these Si isopleths are rather steep and, hence, more restricted *P–T* conditions may be derived from the intersection of the following multivariant equilibria (method 2):

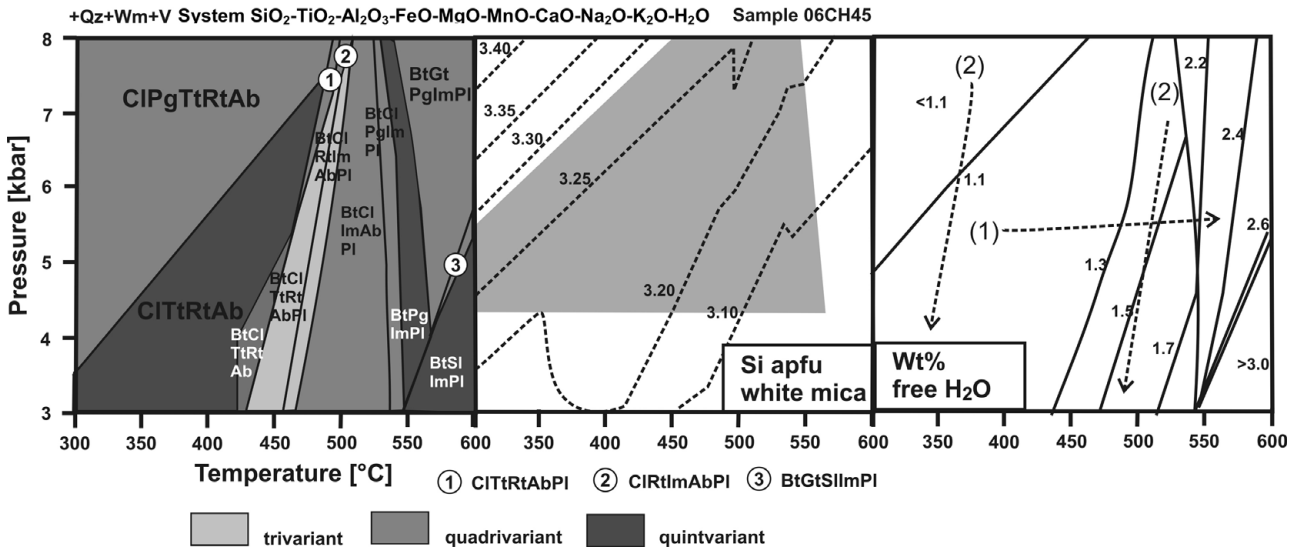

Figure 8. *P–T* pseudosection calculated for phyllite 06CH45 considered characteristic of the CMC metapsammopelite (Table 3) with isolines for Si contents in white-mica and for free water. Inserted grey field represents the estimated *P–T* space where the studied metapsammopelitic rocks equilibrated (see text). (1) and (2) are possible partial PT paths (see explanation in text).

(E1) 60 Mg-Al-celadonite$_{Wm}$ + 7 daphnite$_{Cl}$ + 14 quartz + 12 clinozoisite$_{Ep}$ = 22 H_2O + 12 tremolite$_{Am}$ + 25 muscovite$_{Wm}$ + 35 Fe-Al-celadonite$_{Wm}$

(E2) 25 Mg-Al-celadonite$_{Wm}$ + 7 clinochlore$_{Cl}$ + 14 quartz + 12 clinozoisite$_{Ep}$ = 22 H_2O + 12 tremolite$_{Am}$ + 25 muscovite$_{Wm}$

(E3) 5 Mg-Al-celadonite$_{Wm}$ + daphnite$_{Cl}$ = clinochlore$_{Cl}$ + 5 Fe-Al-celadonite$_{Wm}$

(E4) 25 Fe-Al-celadonite$_{Wm}$ + 12 clinochlore$_{Cl}$ + 14 quartz + 12 clinozoisite$_{Ep}$ = 22 H_2O + 12 tremolite$_{Am}$ + 25 muscovite$_{Wm}$ + 5 daphnite$_{Cl}$

P–T conditions close to 353 °C, 6.2 kbar result from the average mineral compositions in sample 02CH37 given in Table 2, assuming water activity $a_{H_2O} = 1.0$.

The more frequent assemblage 1, with hornblende, white-mica, epidote, plagioclase, chlorite and rutile (02CH42, 06CH55, 06CH63, 07CH23), yielded maximum *P–T* conditions of 500–570 °C, 6–9 kbar according to the position of the Si isopleth for its minimum content of 3.15 Si apfu for white-mica (rim compositions) in the stability field of rutile, plagioclase and hornblende (rim compositions) and above the stability field of biotite. The additional presence of paragonite in sample 02CH42 would indicate pressures exceeding 7.5 kbar. Using average rim compositions (given in Table 2), the intersection of the multivariant reactions E1–E4 results at 518 °C, 8.3 kbar (02CH42) and 575 °C, 6.7 kbar (06CH63), respectively. Actinolite, albite and phengite (3.3 Si apfu) in the cores of amphibole, plagioclase and white-mica in samples of the same assemblage define a previous *P–T* stage. Using average core compositions of minerals in sample 02CH42 (Table 2), the intersection of the multivariant reactions E1–E4 at 412 °C, 9 kbar would represent this stage.

According to the above data, three different *P–T* evolutions were deduced from the collected metabasite samples. Most samples equilibrated within a broadly constrained range of *P–T* conditions at 350–430 °C, 6.2–9 kbar (stage I). Only sample 07CH24 yielded lower peak *P–T* conditions (< 380 °C, < 4.5 kbar). However, minerals related to the *P–T* conditions of stage I could have been completely extinguished. Conditions of stage I coincide with those deduced as peak *P–T* conditions from rocks of the central Chilean accretionary system (Willner, 2005). All samples except 02CH37 underwent nearly isobaric heating at depth to reach peak *P–T* conditions (stage II) at 510–580 °C, 6.6–8.5 kbar.

P–T estimation in the metapsammopelitic rocks of the CMC is not straightforward. The fully recrystallized quartz fabric, where detrital relics are no longer detectable, is similar to quartz fabric type F of Brix *et al*. (2002) in HP–HT metagreywackes. This type is attributed to temperatures exceeding 320–350 °C. Sample 06CH45 is a typical metapsammopelitic rock of the CMC. A *P–T* pseudosection was calculated for the whole-rock composition of this sample to be taken as a petrogenetic grid (Fig. 8). The assemblages and Si contents of white-mica observed in the studied samples allow us to define a wide range of peak *P–T* conditions at 300–550 °C, 4–8 kbar compatible with the conditions of stages I and II deduced from metabasite. Whereas most biotite-free samples did not reach 450 °C, temperatures in biotite-bearing sample 02CH27 must have exceeded 450 °C, and in 06CH54 even 500 °C according to the presence of andesine. Maximum temperatures should have been below 550 °C owing to the lack of garnet. The occurrence of garnet pseudomorphs in biotite-free sample 02CH36 may be explained by a whole-rock composition being more calcic than that of sample 02CH44 (Fig. 9). Then, garnet can crystallize before

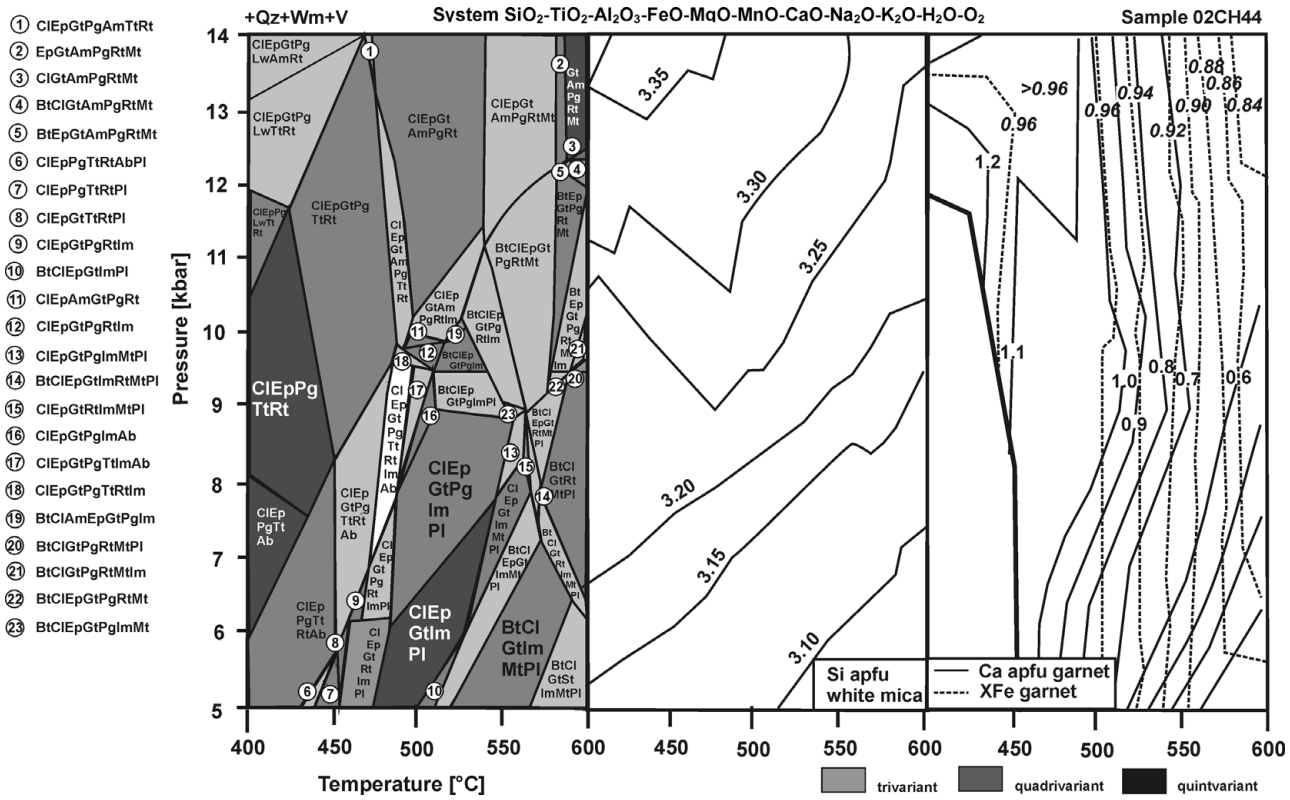

Figure 9. *P–T* pseudosection calculated for the coarse-grained garnet mica-schist 02CH44 (Table 3) with inserted isolines for Si contents in white-mica as well as for Ca contents and X_{Fe} in garnet.

biotite at temperatures exceeding 450 °C and somewhat more.

A *P–T* pseudosection for the unusually coarse-grained garnet mica-schist 02CH44 (Fig. 9) with the assemblage garnet–white-mica–chlorite–epidote–quartz–rutile points to peak *P–T* conditions of 570–585 °C, 11–13 kbar as defined by the Si isopleth of white-mica (3.26 apfu) in the field of chlorite, garnet and epidote and above the *P–T* field of biotite. These *P–T* conditions exceed those of all other rocks of the CMC by far. Isopleths of the Ca contents of garnet (0.45–0.72 apfu) and its X_{Fe} (0.93–0.78) coincide with the temperature ranges, but indicate that maximum temperature and, hence, pressure may have been even somewhat higher than given before. The garnet mica-schist has very similar characteristics to local rocks within the basally accreted levels of the accretionary system at 40° 57′ S (Los Pabilos; Willner *et al*. 2004*a*) and 34° 32′ S (Punta Sirena; Willner *et al*. 2005) that are interpreted to be derived from the subduction channel below the basally accreted levels. The following characteristics that point to the higher pressure, derived for the garnet mica-schist, and, thus, to a different tectonic environment with respect to the surrounding rocks are: (1) highest Si contents in phengite; (2) grossular-rich garnet in assemblage with albite and rutile; (3) retrograde replacement of garnet by white-mica and chlorite. In contrast to the surrounding rocks, this schist is also characterized by pervasive non-coaxial deformation.

4.b.2. Arrayán Formation and Huentelauquén Formation

The low degree of recrystallization and the preservation of the detrital fabric of the metagreywackes in the AF point to relatively low temperatures. The quartz fabric preserved within all rocks of the AF and HF is similar to types B to D of the study by Brix *et al*. (2002). These types are compatible with a temperature range of 280–320 °C. Maximum pressures for the AF are indicated by the highest Si contents in metamorphic white-mica. For K-feldspar-bearing samples (02CH38, 06CH40, 06CH43, 06CH46) pressures can be calculated using the following equilibrium (method 2; Fig. 10):

(E5) 5 Al-celadonite$_{Wm}$ + muscovite$_{Wm}$ = 2 H_2O + 2 quartz + 6 K-feldspar + clinochlore$_{Cl}$

Assuming that maximum pressures were attained during very-low grade metamorphism (200–320 °C) and at $a_{H_2O} = 1$, the calculated pressure range is between 4 and 6 kbar. Such values are comparable with very-low grade frontal accretion systems in Southern Chile such as the Eastern Belt of the Chonos Metamorphic Complex (Willner, Hervé & Massonne, 2000) and the Madre de Dios Metamorphic Complex (Willner *et al*. 2009). Si contents of metamorphic white-mica in the metaconglomerate of the HF are lower (≤ 3.2 apfu), but biotite is present as an indicator of the highest temperature reached. The quartz fabric in the HF is remarkable in that it is identical to that of the AF and, hence, resembles that of very-low grade metamorphism. No reliable temperature

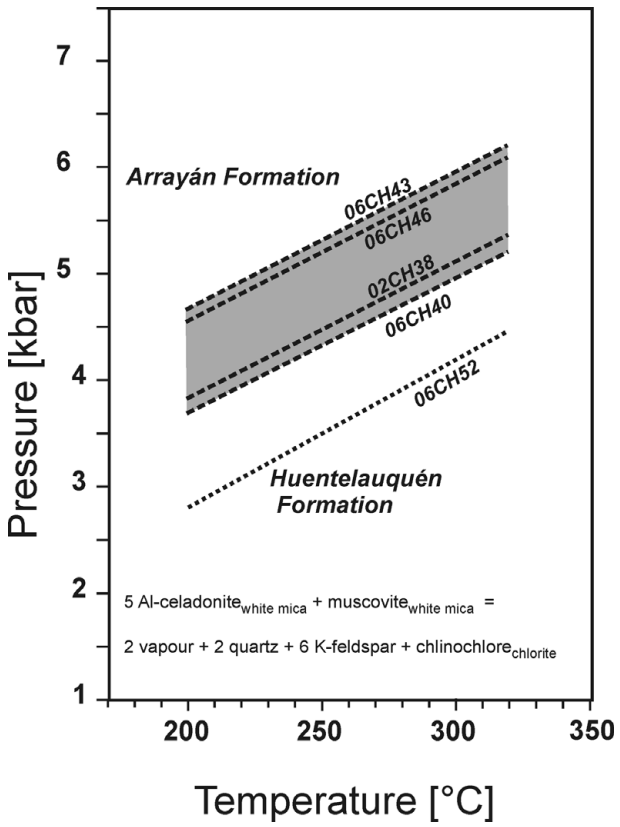

Figure 10. Pressure estimation of K-feldspar and white-mica bearing rocks of the AF and HF.

estimate could be made. But it is assumed here that biotite must have formed at a significantly lower temperature than that predicted for metagreywackes in Figure 8 (430–470 °C). If we additionally assume that maximum pressure was attained during very-low grade metamorphism, pressures may be estimated with equilibrium E5 at 3.0–4.5 kbar (06CH52). Hence, the maximum depth reached by HF rocks was considerably lower than for AF rocks.

4.c. Ar–Ar geochronology

White-mica in 11 samples from the CMC, AF and HF was systematically studied by the *in situ* Ar–Ar UV laser ablation method. The UV laser ablation technique as introduced by Kelley, Arnaud & Turner (1994) allows detection of age heterogeneities at thin-section scale. This is an advantage for studying fine-grained very-low and low grade rocks, where conventional studies of mineral concentrates cannot resolve potential age heterogeneities. The knowledge of the potential age heterogeneity at thin-section scale allows a better assessment of the influence of factors on the K–Ar system like deformation, recrystallization or access of fluids. Considering the used spot size of 50 μm and the average grain size within the samples, it was possible here to analyse single metamorphic grains in the CMC as well as single detrital grains in the AF and HF, whereas clusters of three or four metamorphic grains could only be analysed in the AF. Two types of age information resulted: (1) where single ages do not overlap within their 2σ errors, age ranges are documented; (2) single events can be detected where ages overlap within their 2σ errors and their weighted means are identical to Ar–Ar isochron ages.

4.c.1. The Choapa Metamorphic Complex

Conspicuously, distribution of Ar–Ar ages in the CMC is extremely heterogeneous, spanning over 160 Ma between samples, whereas continuous age intervals of 20–40 Ma are common within samples (Fig. 11; Table 4).

Garnet mica-schist 02CH44 (Fig. 11a; Table 4) shows the oldest continuous age range at 274–307 Ma (ten spot ages), and additionally one spot age at 245 Ma and two spot ages at 198–204 Ma. This oldest age range does not belong to a single age population, where ages overlap within the 2σ errors. Hence, no weighted mean is calculated here. A separately derived plateau age of 303 ± 2 Ma (Fig. 11b; Table 4) by stepwise heating of a single grain of 1 mm diameter is identical to the oldest spot age at 307 ± 3 Ma showing that this age is related to the essential and original age of the grain and most probably related to the age of its core. The spot ages that are younger than 303 Ma (Fig. 11a) are interpreted to have resulted from later white-mica crystallization during exhumation following the studies of Willner *et al*. (2005). In phyllite 06CH45 (Fig. 11c; Table 4), ten spot ages define a similar wide continuous age range at 242–279 Ma that can also be interpreted as a group of single crystallization ages related to continuous white-mica growth during exhumation. The oldest age is related to white-mica growth close to peak metamorphic conditions.

The Ar–Ar age ranges in the greenschist strongly differ from those of the above metapsammopelitic samples: greenschist 02CH42 (Fig. 11d; Table 4) yielded an age range of 188–227 Ma (eight spot ages). However, only the older six spot ages (198–227 Ma) form an age group with single ages overlapping within the 2σ errors. Their weighted average of 210 ± 2 Ma is identical to the normal and inverse isochron ages of 212 ± 5 Ma with the same dataset for the weighted mean and respective initial $^{40}Ar/^{36}Ar$ ratios of 293 ± 5 identical to that of atmospheric Ar (295.5). Two younger spot ages with a weighted average of 188 ± 2 Ma are interpreted to represent a different white-mica crystallization event.

Greenschist 06CH63 (Fig. 11e; Table 4) shows a spot age cluster at 162–181 Ma (six spot ages) and one separate spot age of 136 Ma; the weighted mean of 169 ± 3 Ma of the older spot age group is identical to the normal and inverse isochron ages of 168 ± 5 Ma with data for the same group, with initial $^{40}Ar/^{36}Ar$ ratios of 297 ± 20 (normal isochron) and 298 ± 19 (inverse isochron) identical to that of atmospheric Ar, and most likely represents a single event of white-mica crystallization.

Phyllite 06CH54 (Fig. 11f) yielded the youngest and smallest Ar–Ar spot age range of 127–143 Ma

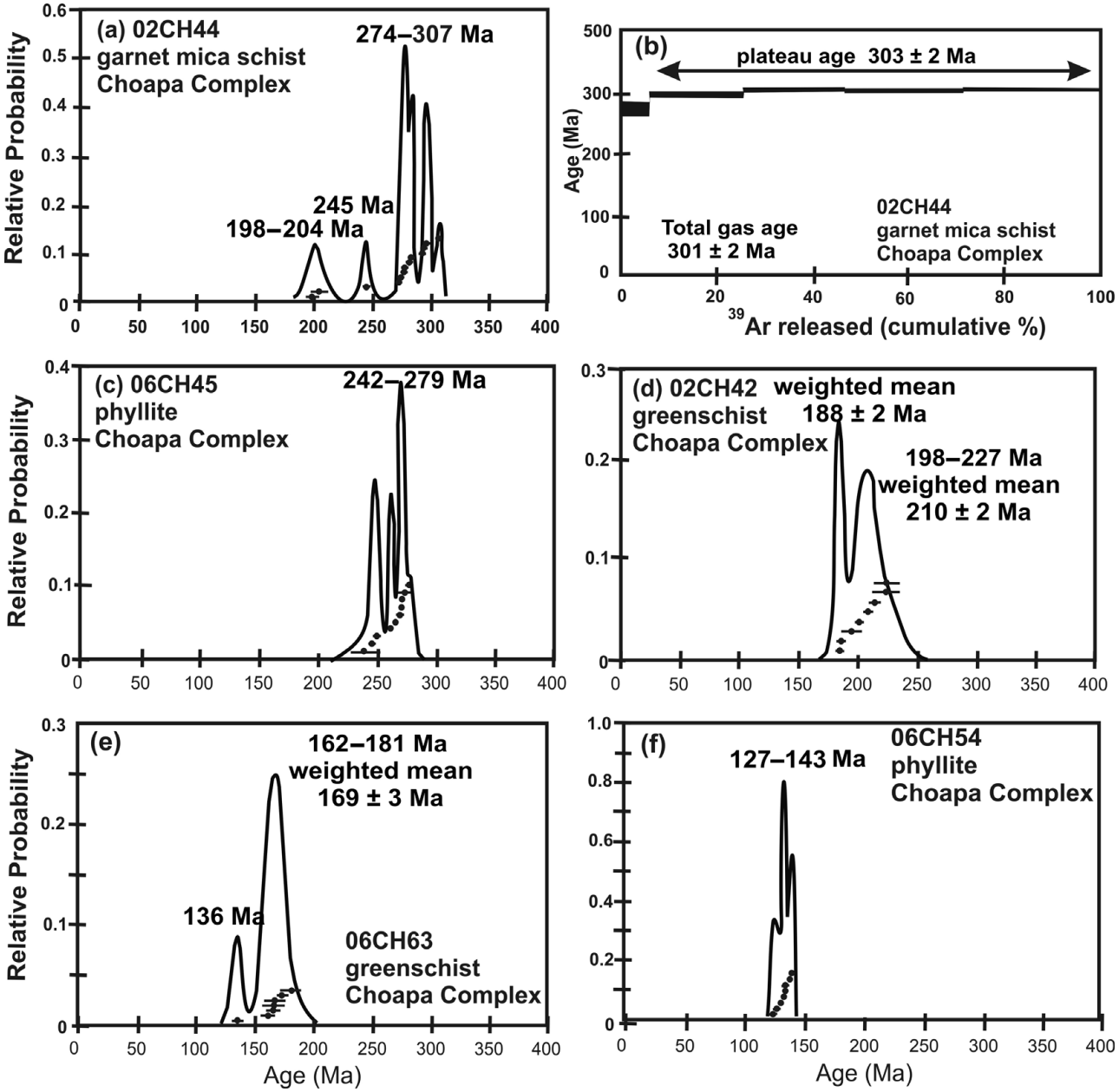

Figure 11. Probability plots for ^{40}Ar–^{39}Ar single-grain laser ablation ages of white-mica from rocks of the CMC including one ^{40}Ar–^{39}Ar release spectrum and plateau age for white-mica in garnet mica-schist 02CH44. The error bars indicate one sigma.

(eight spot ages). However, not all single ages overlap within their 2σ errors, and therefore the calculation of the weighted average of all these ages might not give a meaningful age. Here, spot ages rather represent continuous crystallization of white-mica over a prolonged period of time.

4.c.2. The Arrayan Formation

Ar–Ar spot ages of white-micas in rocks of the AF are represented in Figure 12 and Table 4. The age clusters partly correspond to the younger age clusters in the CMC.

The oldest spot age cluster in the AF results from metapelite 06CH43 (Fig. 12a; Table 4) at 227–251 Ma (seven spot ages). Although this age group represents an apparent single peak in the probability curve, not all single ages overlap within their 2σ errors and therefore no weighted mean is calculated. Again this age group represents a continuous crystallization of white-mica over a prolonged period of time.

Metagreywacke 02CH43 (Fig. 12b; Table 4) yielded the widest spot age range of 207–257 Ma (eight spot ages) showing a bimodal distribution with weighted means at 207 ± 7 Ma (calculated with the three younger ages) and 245 ± 4 Ma (calculated with the older five ages). The latter age agrees with the isochron ages of 251 ± 8 Ma (normal isochron) and 253 ± 5 Ma (inverse isochron) within their errors, with respective initial $^{40}Ar/^{36}Ar$ ratios at 276 ± 15 (normal isochron) and 275 ± 14 (inverse isochron) compatible with atmospheric Ar within 2σ errors.

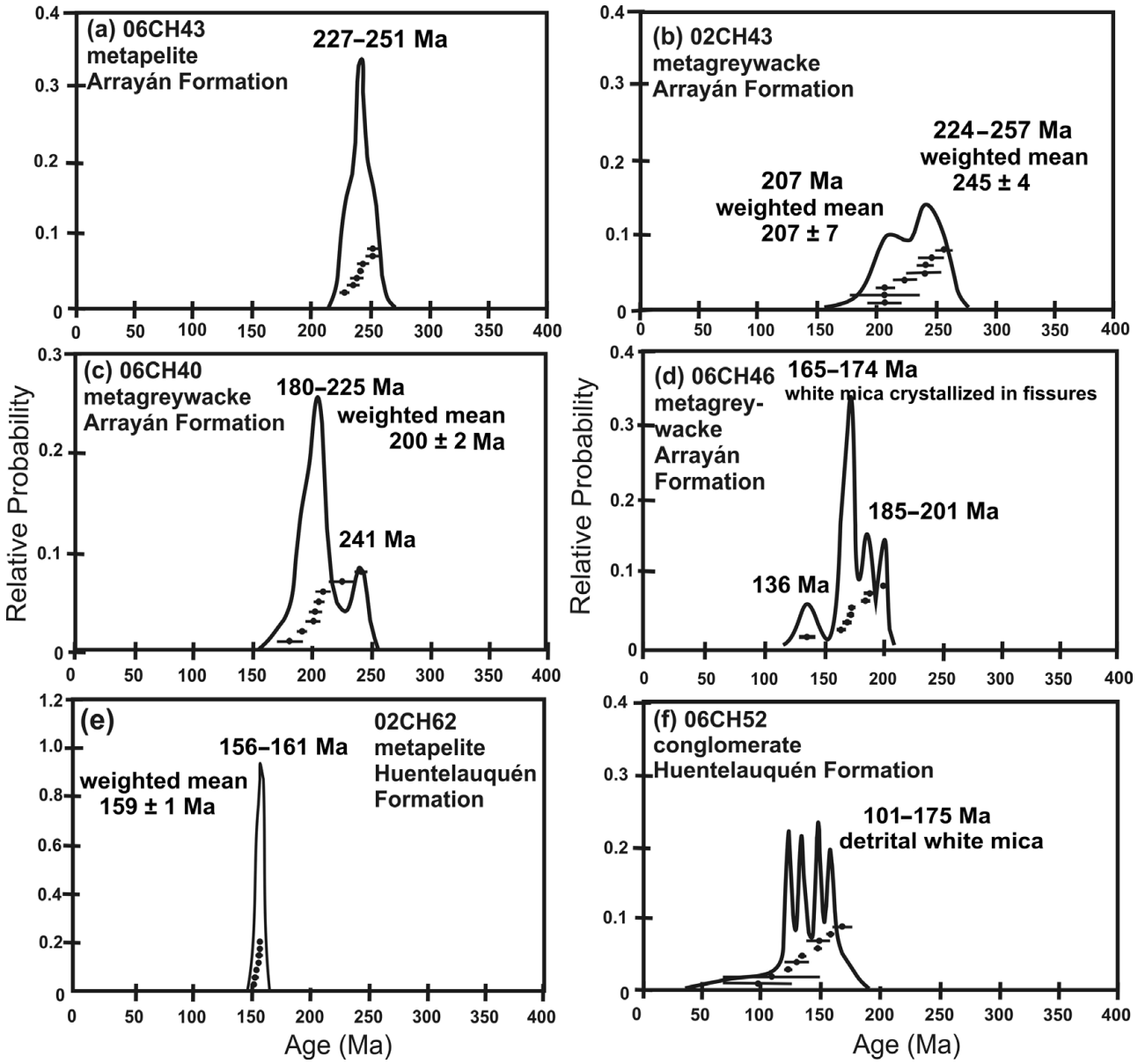

Figure 12. Probability plots for ^{40}Ar–^{39}Ar single-grain laser ablation ages of white-mica from rocks of the AF and HF. The error bars indicate one sigma.

In metagreywacke 06CH40 (Fig. 12c; Table 4), seven spot ages determined from detrital as well as metamorphic white-mica result in a homogeneous age range of 180–225 Ma (seven spot ages) and one spot age of 241 Ma. The weighted mean at 200 ± 2 Ma of the younger peak is identical with isochron ages at 200 ± 6 Ma (normal isochron) and 203 ± 6 Ma (inverse isochron). Respective initial $^{40}Ar/^{36}Ar$ ratios of 287 ± 19 and 287 ± 18 are identical to that of atmospheric Ar within errors.

The most heterogeneous ages were obtained from the cataclastically deformed metagreywacke sample 06CH46 (Fig. 12d; Table 4). Four spot ages were measured in fine-grained white-mica within fissures resulting in a narrow age range of 165–174 Ma, whereas minor age peaks are detected in clusters of metamorphic white-mica at 185–201 Ma (three spot ages) and 136 Ma (one spot age). Only the first cluster appears to be a single event of white-mica crystallization with a weighted mean at 171 ± 2 Ma corresponding to isochron ages of 181 ± 5 Ma (normal and inverse isochrons). However, their respective initial $^{40}Ar/^{36}Ar$ ratios of 257 ± 17 are lower than the atmospheric value beyond their 2σ errors. The assumption of single initial atmospheric $^{40}Ar/^{36}Ar$ ratios for those four spot ages is obviously not correct in this case, and crystallization of the white micas in the fissures occurred during a longer period of time.

4.c.3. The Huentelauquén Formation

White-mica in the HF shows the youngest age clusters (Fig. 12; Table 4). In metapelite 02CH62 (Fig. 12e; Table 4), seven spot ages of fine-grained metamorphic white-mica define a narrow range at 156–161 Ma around a weighted mean of 159 ± 1 Ma that is identical

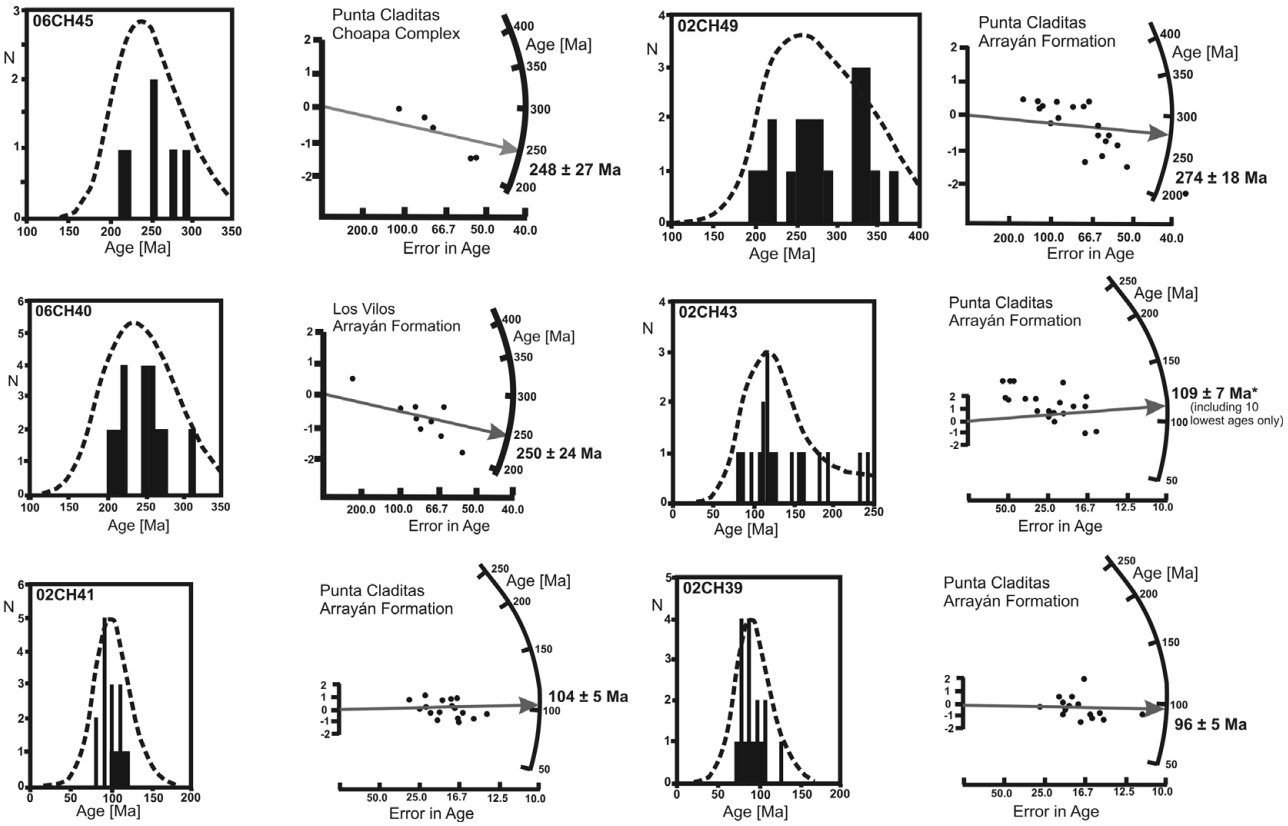

Figure 13. Histogram and radial plot representation of zircon single-grain FT age data for selected rocks of the study area.

to the isochron ages of 166 ± 6 Ma (normal isochron) and 167 ± 6 Ma (inverse isochron) within 2σ errors, with respective initial $^{40}Ar/^{36}Ar$ ratios of 255 ± 32 and 250 ± 32, which are lower but agree with atmospheric value within 2σ errors.

Only single detrital white-mica grains were measured in conglomerate 06CH52 (Fig. 12f; Table 4) yielding a wide continuous spot age range from 101 to 175 Ma. These are single ages of white-mica crystallization. Hence, no weighted mean is calculated here.

4.d. Fission-track geochronology

Concentrates of detrital zircon from seven metagreywacke samples (two from the CMC, five from the AF) were dated by the FT method. Individual ages were determined by calculating a central age (Galbraith & Laslett, 1993) from up to 20 individual grain ages. The single-grain FT age data for each sample are described by their age dispersion and are graphically presented by radial plots (Galbraith, 1990; Fig. 13; Table 5).

Zircon FT ages also show a remarkable scatter. However, two groups may be distinguished:

(1) Four central ages belong to the oldest FT ages so far recorded in the metamorphic basement of the Chilean coastal range similar to those recorded by Thomson & Hervé (2002) for the Eastern Andean Metamorphic Complex in Patagonia, a frontal accretion system of similar age, and *P–T* and structural record (sample number and unit in brackets): 274 ± 18 Ma (02CH49; AF), 272 ± 40 Ma (06CH54; CMC), 250 ± 24 Ma (06CH40; AF) and 248 ± 27 Ma (06CH45; CMC). This indicates that parts of the studied area had cooled below ∼ 280 °C already during Permian times. The latter two ages are identical for the CMC and the AF, but show very high errors of individual ages (217 ± 65 Ma to 314 ± 135 Ma). The oldest age of 274 ± 18 Ma in sample 06CH49 derived from 20 individual ages is even more complex; individual ages are also characterized by high errors and altogether, a wide age range (368 ± 145 Ma to 203 ± 69 Ma). Eight of 20 individual ages show ages exceeding 310 Ma. This means that cooling below ∼ 280 °C may have started before 310 Ma and ages were partially reset. Thus, the central age of 274 ± 18 Ma must be regarded with caution. A similar age of 272 ± 40 Ma from the CMC is based on a single measurement only.

(2) FT dating of three samples from a regionally restricted part of the AF (Fig. 2) yielded surprisingly young ages of 96 ± 5 Ma (02CH39), 104 ± 5 Ma (02CH41) and 110 ± 7 Ma (02CH43). Whereas the first two samples show a relatively narrow range of individual ages (75 ± 17 Ma to 131 ± 17 Ma), the latter sample (02CH43) shows a wide range of individual ages between 281 ± 56 Ma and 87 ± 15 Ma that indicates strong partial resetting of ages within this sample. The relict ages point to the older post-metamorphic cooling history of this sample. The central age of this sample was derived from the ten youngest individual ages only.

5. Discussion

5.a. Geochronology of the Choapa Metamorphic Complex

Only two rocks in the CMC (garnet mica-schist 02CH44 and phyllite 06CH45) yielded Ar–Ar ages that are older than the time of the first Mesozoic intrusions into the accretionary wedge at 31° S (220 ± 20 Ma and 200 ± 10 Ma; Irwin *et al*. 1988). These intrusions set an important time mark for the end of the accretion process in central Chile (see also Willner *et al*. 2005; Glodny *et al*. 2006). The Ar–Ar spot age variations in both rocks show very similar patterns to those derived from equivalent rocks of the basally accreted Western Series at lat. 34–35° S (Willner *et al*. 2005) that was largely unaffected by postaccretional resetting. Because peak temperature of the typical metagreywacke sample 06CH45 was near or below the closure temperature of the K–Ar system, its oldest recorded age of 279 ± 3 Ma can be interpreted as a white-mica crystallization age, which approximately dates the peak of HP–LT metamorphism at 350–430 °C, 6.2–9.0 kbar (stage I). We interpret the continuously younger ages until 242 ± 12 Ma as the result of crystallization of compositionally zoned white-mica by mineral reactions and static growth during cooling and exhumation significantly after the accretion process. This interpretation follows studies of *P–T* paths in equivalent rocks at lat. 34–35° S (Willner, 2005; Willner *et al*. 2005). Here, the youngest age probably represents cooling below ∼ 300 °C, when the progress of retrograde reactions during the exhumation path ended. Willner (2005) and Massonne & Willner (2008) calculated free water isopleths within *P–T* pseudosections at very-low to low grade showing that water is internally generated during the decompression path to trigger continuous metamorphic reactions. On the other hand, the garnet mica-schist 02CH44, which formed at considerably higher peak metamorphic conditions of 570–585 °C, 11–13 kbar, also shows the oldest spot age range of 274–307 Ma. The oldest age of 307 ± 3 Ma, which is confirmed by a plateau age of 303 ± 2 Ma of a single large grain, presumably also dates formation of the core of the white-mica. Continuously younger ages until 274 ± 2 Ma would correspond to the crystallization of compositionally zoned white-mica by mineral reactions during further cooling and exhumation to the level of the basal accretion system, where the first white-mica of sample 06CH45 formed. If mere volume diffusion during cooling to the closure temperature would apply, no such age range would have been preserved. During joint exhumation within the basally accreted rocks, white-mica formation continued in garnet mica-schist 02CH44 at 245 ± 3 Ma, which is identical to the youngest age recorded in sample 06CH45. The minor cluster at 204–198 Ma is interpreted to be owing to incipient Mesozoic resetting at presumably an even lower temperature. Following similar findings by Willner *et al*. (2004*a*) and Willner (2005), the exotic intercalation of garnet mica-schist in the CMC with the highest *P–T* conditions and oldest ages can be interpreted as being derived from the subduction channel below the mantle wedge of the convergent margin. Hence, in both rocks (06CH45 and 02CH44) about 35–40 Ma of retrograde mineral formation during exhumation are documented. A zircon FT age of 248 ± 27 Ma in metagreywacke sample 06CH45 represents the first cooling below ∼ 280 °C and is equivalent to the youngest Ar–Ar white-mica ages in the same rock. A zircon FT age of 272 ± 40 Ma for metagreywacke 06CH54 is not in conflict with this view.

The remaining three samples from the CMC show younger age clusters with weighted means at 188 ± 2 Ma, 210 ± 2 Ma (02CH42) and 169 ± 3 Ma (06CH63) and a continuous age range of 143–127 Ma (06CH54). These ages are younger than the time of the first Mesozoic intrusions into the accretionary wedge at 31° S (220 ± 20 Ma and 200 ± 10 Ma; Irwin *et al*. 1988), the FT age of 248 ± 27 Ma (sample 06CH45) and the first regional unconformity in the area at ∼ 245 Ma (base of the Anisian). Hence, these younger ages represent ages of a late resetting of the Ar–Ar system within near-surface levels. This resetting is also unrelated to the isobaric heating to conditions of 510–580 °C, 6.6–8.5 kbar (stage II) that was observed in all three rocks. This thermal overprint most likely occurred before exhumation to near-surface levels that was largely finished at around 245 Ma.

5.b. Geochronology of the Arrayán and Huentelauquén formations

The Ar–Ar age clusters of four samples from the AF (227–251 Ma, 06CH43; 207–257 Ma, 02CH43; 180–241 Ma,06CH40; 136–201 Ma, 06CH46) and of the two samples from the HF (156–161 Ma, 02CH62; 101–175 Ma, 06CH52), which include detrital and metamorphic white-mica, are also uniformly younger than the first unconformity above these formations at ∼ 245 Ma (base of the Anisian). The weighted mean of 245 ± 4 Ma in sample 02CH43, the age peak at 227–251 Ma in sample 06CH43 and the oldest spot age of 241 ± 6 Ma in sample 06CH40 are identical within errors and represent the oldest recorded Ar–Ar spot ages in the AF similar to the age of the unconformity. Thus, all recorded Ar–Ar spot ages in the AF and HF are unrelated to the peak of metamorphism and must be interpreted as age resettings at different times and at different, but nearby localities within both formations. Resetting events are approached to variable degrees. In sample 02CH43, spot ages mark two separate resetting events with two weighted means at 245 ± 4 Ma and 207 ± 7 Ma. On the other hand, only one single resetting event with a weighted mean of 159 ± 1 Ma is recorded in metapelite 02CH62 with a narrow age spectrum.

Most remarkably, resetting in the AF and HF definitely occurs below the closure temperature of the K–Ar system. This means that Ar loss by volume diffusion can play only a minimum role in the resetting

event. Grain size has no effect on resetting, because detrital white-mica in samples 06CH40 and 06CH52, which has far larger grain sizes than metamorphic white-mica, yielded the same range of reset ages, far younger than the sedimentation ages. Deformation as a factor of resetting can only be discussed for the cataclastically deformed sample 06CH46 from a compressive sinistral strike-slip zone. Fissures caused by the strike-slip event can be dated using white-mica formed within these fissures (Fig. 3d). Such mica crystallized during the age period 174–165 Ma, whereas resetting of larger white-mica outside the fissures could have been caused by Ar release owing to grain deformation.

Also surprising is the fact that zircon FT ages are older than Ar–Ar white-mica ages in the AF as in the case of sample 06CH40, where the zircon FT age of 250 ± 24 Ma indicates cooling below $\sim 280\,^{\circ}$C. This contrasts with the usual sequence of older white-mica Ar–Ar ages and younger zircon FT ages as evidenced, for example, by CMC sample 06CH45. These findings show that temperatures during resetting of the Ar ages could have been below $\sim 280\,^{\circ}$C.

Finally, the original question remains: when did the metamorphic peak and accretion occur in the AF? This may be vaguely approximated by the single FT ages recorded in sample 06CH49. Owing to the large spread of single zircon FT ages and their large errors, the high central age at 274 ± 18 Ma does not seem to be meaningful, because strong partial resetting of FT ages appears to have occurred in this sample. It is notable that 8 out of 20 single FT ages are older than 310 Ma. However, their single errors are very large. The age mark of ≥ 310 Ma can only be taken as a very vague hint at the original cooling FT age of zircon after metamorphism. If so, it can be assumed that accretion and very-low grade metamorphism of the frontally accreted AF presumably occurred before 310 Ma. This would concur with the findings of Richter *et al*. (2007), Willner *et al*. (2005) and Willner, Gerdes & Massonne (2008) that frontal accretion occurred before basal accretion in central Chile.

5.c. Interpretation of age resetting events

Summarizing the above findings, we propose that the reset Ar–Ar ages in the AF and HF samples must represent ages of white-mica recrystallization during access and presence of hydrous fluids at temperatures below $\sim 280\,^{\circ}$C. However, shape and orientation of the former white-mica did not change, as it can be observed particularly for detrital white-mica. Element distribution maps of detrital white-mica (Fig. 6) show that compositional changes occurred, spreading from the rims and along the cleavage planes of white-mica to its centre. We envisage an *in situ* dissolution/precipitation effect by hydrous fluids penetrating the rocks at different times and depths. Figure 6 shows that low Si, Fe, Mg versus high Ti detrital white-mica (probably of magmatic origin) is replaced by higher Si, Fe, Mg versus lower Ti white-mica in AF sample 06CH40 (Fig. 6a, b). Conversely high Si, Fe, Mg, Ti detrital white-mica (probably of HP–LT origin) is replaced by lower Si, Fe, Mg, Ti white-mica (probably at LP–LT conditions) in HF sample 06CH52. Resetting of detrital white-mica does not only occur in the original source rocks (e.g. Reynolds, Barr & White, 2009), but also in the sediment at low temperature or even diagenetic conditions leading to ages younger than the sedimentation age (e.g. Willner *et al*. 2004*b*). Ramírez-Sánchez, Deckart & Hervé (2007) and Willner *et al*. (2009) proved low temperature resetting of white-mica in very-low grade accretionary prisms in Southern Chile. McDowell & Elders (1980) reported 'illitization' of muscovite in the Salton Sea System borehole at temperatures $\leq 280\,^{\circ}$C causing an apparent younging of ages. This process would imply partial or complete replacement of potassic white-mica by potassic white-mica with a distinct composition. Also the clearly defined ages of resetting in those clusters, where spot ages can be defined by a weighted average identical to isochron ages (samples 02CH42, 06CH63, 02CH43, 06CH40, 06CH46 and 02CH62), would rather point to *in situ* dissolution/precipitation compared to a possible alternative of merely a solution of Ar within the white-mica interlayer position. Removal of Ar from the white-mica would rather result in unsystematic patterns.

The resetting of Ar–Ar ages in the AF and HF can be correlated with specific geological events. For instance, we regard the zircon FT ages of 250 ± 24 Ma (06CH40) and 248 ± 27 Ma (06CH45) as ages of cooling under $\sim 280\,^{\circ}$C for the AF and the CMC, respectively. These ages are similar to the age of the first unconformity above the AF under the Anisian cover (*c*. 245 Ma). The above mentioned oldest Ar–Ar reset ages at 245–241 Ma determined for samples 02CH43, 06CH43 and 06CH40 are also related to this event. Presumably, white-mica in the entire AF and HF was originally reset at this time. Furthermore, the weighted means of 210 ± 2 Ma in sample 02CH42, 207 ± 7 Ma in sample 02CH43 and 200 ± 2 Ma in sample 06CH40, as well as the oldest spot age in sample 06CH46 at 201 ± 3 Ma, are equivalents to the 220–200 Ma event of bimodal intrusions, extension and heating also recorded in the CMC (Irwin *et al*. 1988; Willner *et al*. 2005; Glodny *et al*. 2006). We interpret these ages as low temperature resetting at shallow depth within local blocks in the AF similar to the pattern observed in the CMC. Also the dated strike-slip event at 174–165 Ma (06CH46) has an age equivalent at 169 ± 3 Ma in the CMC (06CH63) and presumably at 159 ± 1 Ma in the HF (02CH62). An even younger resetting is recorded by the three young zircon FT ages at 109–96 Ma in samples 02CH41, 02CH43 and 02CH39. In the corresponding locally restricted area SW of Punta Tomás, cooling under $\sim 280\,^{\circ}$C occurred as late as Early Cretaceous times, and hence this block was presumably the latest to be exhumed in the study area. Nevertheless, other causes of resetting, e.g.

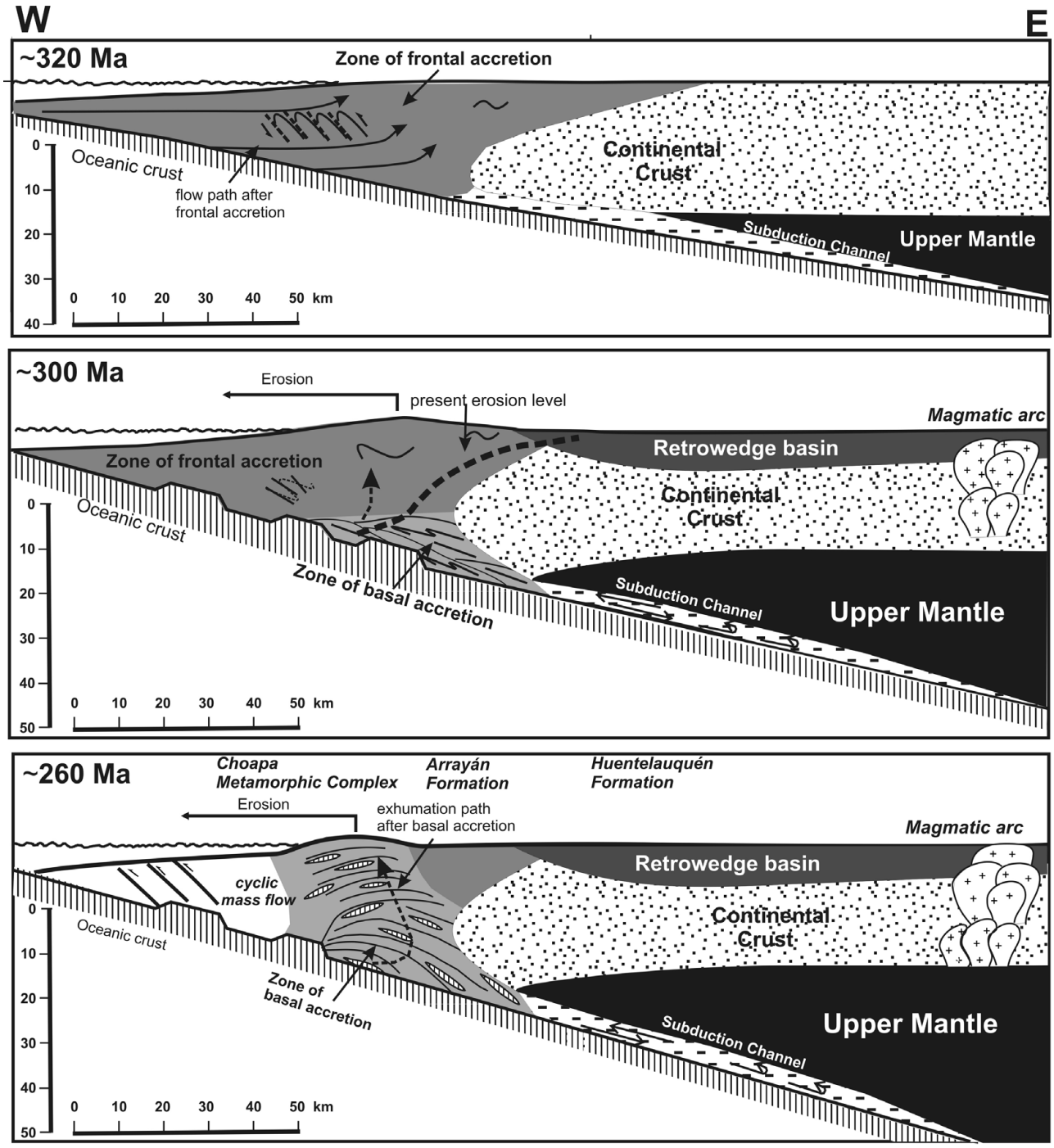

Figure 14. Principal structure and evolution of the late Palaeozoic fore-arc system in central Chile at lat. 31–32° S. A continuous change of the accretion mode from frontal to basal accretion occurred (Richter *et al*. 2007). Frontal accretion is characterized by horizontal particle flow paths and shortening, folding of bedding, thrusting and by sub-vertical foliation. Basal accretion is characterized by vertical shortening and particle flow paths as well as sub-horizontal foliation, intrafolial folds and duplex structures.

hydrothermal convection along faults, might also have been possible.

5.d. Evolution of the late Palaeozoic fore-arc system at lat. 31–32° S

The dating of petrologically well-studied samples by integrated geochronological methods from three different levels of a strongly, but heterogeneously overprinted fore-arc system allows us to unravel the detailed history of successive processes during late Palaeozoic to Mesozoic times. The evolution of the late Palaeozoic fore-arc system is visualized in Figure 14.

(1) This evolution starts with deposition of greywackes and pelites of the AF at $\leq$ 343–337 Ma on a passive continental margin (Willner, Gerdes & Massonne, 2008). In this study we could vaguely approximate the peak of very-low grade metamorphism of the AF (280–320 °C, 4–6 kbar) at > 310 Ma (sample

02CH49). Hence, the first change to convergent margin conditions in central Chile and to frontal accretion of the AF must have occurred within the time interval of 343–310 Ma.

(2) Within the time interval 307 ± 3 Ma to 274 ± 2 Ma, early subducted material (garnet mica-schist 02CH44) ascended from the subduction channel below the mantle wedge (peak conditions: 570–585 °C, 11–13 kbar) to the base of the accretionary prism. A change of the accretion mode from frontal accretion (AF) to basal accretion (CMC) was proposed by Willner, Gerdes & Massonne (2008) at ≥ 308 Ma. Deposition of the metapsammopelites of the CMC started at ≤ 308 Ma and deposition of the sediments of the HF at ≤ 303 Ma (Willner, Gerdes & Massonne, 2008) in a retrowedge basin. The HF received detritus from the rising and eroding CMC (phyllite and phengite clasts) in the west and from a Carboniferous magmatic complex in the east (rhyolite and leucogranite pebbles; Willner, Gerdes & Massonne, 2008). The calcalkaline magmas of the late Palaeozoic magmatic arc (Elqui-Limari batholith; Fig 1a) intruded the retrowedge basin further to the east of the study area in the time interval 310 ± 8 Ma to 256 ± 10 Ma (Rb–Sr whole-rock isochrones; Mpodozis & Kay 1992; Pankhurst, Millar & Hervé, 1996).

(3) At 279 ± 3 Ma (phyllite 06CH45) basal accretion of now-exposed levels of the CMC was ongoing, and HP–LT metamorphism occurred at conditions of 350–430 °C, 6.2–9.0 kbar (stage I). As shown in equivalent rocks at lat. 34–40° S (Willner *et al*. 2005; Glodny *et al*. 2005), exhumation occurred by erosion as the prime exhumation mechanism, outbalanced by continuous basal accretion at the base of the accretionary prism. Cooling of the now-exposed rocks of the CMC below ∼ 280–300 °C occurred until ∼ 248–242 Ma (06CH45; 02CH44). At the same time (∼ 244–240 Ma), Ar–Ar white-mica ages in rocks at the now-exposed base of the AF were entirely reset (06CH43, 02CH43, 06CH40), and the first unconformable deposition onto the AF and HF occurred at ∼ 245 Ma (base of the Anisian El Quereo Formation; Rebolledo & Charrier, 1994). We propose that the end of accretion occurred at that time at lat. 31–32° S. However, accretion must have ended even earlier, as isobaric heating of some rocks (02CH42, 06CH55, 06CH63, 07CH23) to conditions of 510–580 °C, 6.6–8.5 kbar (stage II) and exhumation of these rocks also ended at ∼ 245 Ma. This also means that this heating may have been related to a magmatic arc at depth that is not exposed and possibly intruded the accretionary prism slightly before exhumation to near-surface levels.

(4) At 220 ± 20 Ma to 200 ± 10 Ma, the earliest detectable intrusion of bimodal plutons into the (now-exposed) accretionary prism occurred at lat 31° S (Rb–Sr whole-rock isochrones; Irwin *et al*. 1988). This event can be recognized throughout central Chile and is related to a major change to extensional conditions at the convergent Pacific margin of central Chile (Vásquez & Franz 2008; Willner *et al*. 2005; Glodny *et al*. 2006; Charrier, Pinto & Rodríguez, 2007). Also, Ar–Ar ages of white-mica were locally reset in the CMC and AF in the presence of fluids in the interval of 210 ± 2 Ma to 200 ± 2 Ma (02CH42, 02CH43, 06CH40 06CH46).

(5) We dated a Jurassic compressive sinistral strike-slip event (Ring *et al*. 2011) at 174–165 Ma. The strike-slip zones are the dominant structures in the Bahia Agua Dulce area (Fig. 2; Rebolledo & Charrier 1994; Ring *et al*. 2011) and are probably the southernmost expression of the Atacama Fault System (Charrier, Pinto & Rodríguez, 2007; Ring *et al*. 2011). This event is mainly responsible for the telescoping of the late Palaeozoic fore-arc at lat. 31–32° S to a short distance. Reset Ar–Ar ages at 169 ± 3 Ma in the CMC (06CH63) and at 159 ± 1 Ma in the HF (02CH62) are probably related to this event.

(6) Local Early Cretaceous resetting ages at 142–127 Ma in the CMC (06CH54; 06CH63) and the HF (06CH46) are time-equivalents to an intra-arc extensional event described outside our study area (Charrier, Pinto & Rodríguez, 2007 and references therein) and might be related to it. However, we could detect no further evidence of extension at that time in our study area so far (Ring *et al*. 2011).

(7) Zircon FT ages in the time interval 110 ± 7 Ma to 96 ± 5 Ma of rocks (02CH43, 02CH39 and 02CH41) within a restricted area of the AF SW of Punta Tomás (Fig. 2) can be related to local latest cooling under ∼ 280 °C in the study area. A Mid-Cretaceous compressive event is widespread in central Chile (e.g. Arancibia, 2004; Willner *et al*. 2005) and responsible for the closure of Mesozoic basins. It can be assumed that the local zone with the youngest zircon FT ages was exhumed along a compressional fault.

6. Conclusions

The late Palaeozoic fore-arc system at 31–32° S shows conspicuous heterogeneities of ages and *P–T* conditions owing to present-day exposure of different environments of the fore-arc system over a short distance. These heterogeneities are mostly owing to various low temperature age resettings related to Mesozoic extensional and compressional events within a magmatic arc setting on a long-lived convergent margin. Although the rocks of the late Palaeozoic fore-arc system form inliers within the Mesozoic arc, a pervasive heating event can be excluded, as, for example, at lat. 34–40° S, where the early frontally accreted rocks (Eastern Series) were overprinted by a LP–HT event around the Late Carboniferous coastal batholith (Willner, 2005). In the basally accreted CMC, Ar–Ar spot ages can generally be interpreted as crystallization ages by a penetrative metamorphic overprint at 350–430 °C, 6.2–9.0 kbar and subsequent decompression during exhumation at 279–242 Ma or partly during isobaric heating of deep levels of the CMC at 510–580 °C, 6.6–8.5 kbar. Furthermore, an intercalated exotic garnet mica-schist within the

CMC (peak conditions: 570–585 °C, 11–13 kbar) was exhumed from the subduction channel to the base of the accretionary system, where Ar–Ar crystallization ages of white-mica trace the ascent of this intercalation at 307–274 Ma. We envisage the presence of hydrous fluids during the growth of white-mica. These fluids were internally generated by dehydration during prograde heating as well as decompression.

Local resetting of white-mica Ar–Ar ages in the CMC and of all white-mica Ar–Ar ages in the AF (peak metamorphic conditions 280–320 °C, 4–6 kbar) and the HF (peak metamorphic conditions 280–320 °C, 3–4 kbar) occurred below the closure temperature of the K–Ar system related to various Mesozoic events. *In situ* dissolution/precipitation in white-mica grains in contact with hydrous locally penetrating fluids is envisaged as the prime mechanism of resetting. Ar–Ar resetting events mainly occurred at ∼ 245–240 Ma, ∼ 210–200 Ma, ∼ 174–159 Ma and ∼ 142–127 Ma, and a local resetting of FT ages at ∼ 109–96 Ma. All resetting ages correspond to known extensional or compressional Mesozoic events. The age of peak metamorphism in the AF may only vaguely be approximated at > 310 Ma. This is compatible with the observed field relationship that frontal accretion occurred prior to basal accretion in central Chile (Richter *et al*. 2007).

Not only is the original architecture of the late Palaeozoic fore-arc system in north-central Chile strongly modified by Mesozoic extensional and compressional events; its age archive also is. In spite of various resetting events of Ar–Ar ages of white-mica, the original *P–T–t* evolution of the fore-arc system can still be reconstructed, but there is also a chance to deduce its postaccretional Mesozoic history at the long-lived convergent Pacific margin.

Acknowledgements. This work was financed by Deutsche Forschungsgemeinschaft (grant Ma1160/24) and the German–Chilean BMBF–CONICYT co-operation project (Chl 01A 6A). Constructive reviews by J. Glodny and R. Kryza improved the manuscript. S. Rebolledo (Santiago de Chile) introduced us to the study area and R. Charrier (Santiago de Chile) supported with numerous discussions. F. Hansen and D. Dettmar (Bochum) prepared specimens for geochronology. Thanks to all of them.

References

AGUIRRE, L., HERVÉ, F. & GODOY, E. 1972. Distribution of metamorphic facies in Chile: an outline. *Krystallinikum* **9**, 7–19.

ARANCIBIA, G. 2004. Mid-Cretaceous crustal shortening: evidence from a regional-scale ductile shear zone in the Coastal Range of central Chile (32°S). *Journal of South American Earth Sciences* **17**, 209–26.

BERMAN, R. G. 1988. Internally-consistent thermodynamic data for minerals in the system Na_2O-K_2O-CaO-MgO-FeO-Fe_2O_3-Al_2O_3-SiO_2-TiO_2-H_2O-CO_2. *Journal of Petrology* **29**, 445–522.

BERMAN, R. G. 1990. Mixing properties of Ca-Mg-Fe-Mn garnets. *American Mineralogist* **75**, 328–44.

BROWN, T. H., BERMAN, R. G. & PERKINS, E. H. 1989. Ge0-Calc: Software package for calculation and display of pressure-temperature-composition phase diagrams using an IBM or compatible Personal Computer. *Computers & Geoscience* **14**, 279–89.

BRIX, M. R., STÖCKHERT, B., SEIDEL, E., THEYE, T., THOMSON, S. N. & KÜSTER, M. 2002. Thermobarometric data from a fossil zircon partial annealing zone in high pressure-low temperature rocks of eastern and central Crete, Greece.*Tectonophysics* **349**, 309–26.

CONNOLLY, J. A. D. 1990. Multivariable phase diagrams; an algorithm based on generalized thermodynamics. *American Journal of Science* **290**, 666–718.

CONNOLLY, J. A. D. 2005. Computation of phase equilibria by linear programming: a tool for geodynamic modeling and its application to subduction zone decarbonation. *Earth and Planetary Science Letters* **236**, 524–41.

CHARRIER, R., PINTO, L. & RODRÍGUEZ, M. P. 2007. Chapter 3 Tectonostratigraphic evolution of the Andean orogen in Chile. In *The Geology of Chile* (eds T. Moreno & W. Gibbons), pp. 21–114. London: The Geological Society.

DALE, J., POWELL, R., WHITE, R. W., ELMER, F. L. & HOLLAND, T. J. B. 2005. A thermodynamic model for Ca–Na clinoamphiboles in Na_2O–CaO–FeO–MgO–Al_2O_3–SiO_2–H_2O–O for petrological calculations. *Journal of Metamorphic Geology* **23**, 771–91.

EVANS, B. W. 1990. Phase relations of epidote-blueschists. *Lithos* **24**, 3–23.

GALBRAITH, R. F. 1990. The radial plot: graphical assessment of spread in ages. *Nuclear Tracks and Radiation Measurements* **17**, 207–14.

GALBRAITH, R. F. & LASLETT, G. M. 1993. Statistical models for mixed fission-track ages. *Nuclear Tracks* **21**, 459–70.

GLODNY, J., ECHTLER, H., FIGUEROA, O., FRANZ, G., GRÄFE, K., KEMNITZ, H., KRAMER, W., KRAWCZYK, C. M., LOHRMANN, J., LUCASSEN, F., MELNICK, D., ROSENAU, M. & SEIFERT, W. 2006. Long-term geological evolution and mass-flow balance of the South-Central Andes. In *The Andes – Active Subduction Orogeny* (eds O. Oncken, G. Chong, G. Franz, P. Giese, H.-J. Götze, V. Ramos, M. Strecker & P. Wigger), pp. 401–28. Springer.

GLODNY, J., LOHRMANN, J., ECHTLER, H., GRÄFE, K., SEIFERT, W., COLLAO, S. & FIGUEROA, O. 2005. Internal dynamics of a paleoaccretionary wedge: insights from combined isotope tectonochronology and sandbox modelling of the south-central Chilean fore-arc. *Earth and Planetary Science Letters* **231**, 23–39.

GODOY, E. 1984. Reflexiones acerca de transiciones metamorficas en el basamento de Chile central-sur. *Revista Geológica de Chile* **23**, 79–86.

GODOY, E. & CHARRIER, R. 1991. Antecedentes mineralogicos para el origen de las metabasitas y metacherts del Complejo Metamórfico del Choapa (Región de Coquimbo, Chile): un prisma de acreción Palaeozoico Inferior. *Actas 6. Congreso Geológico Chileno*, 410–14.

GONZÁLEZ BONORINO, F. 1971. Metamorphism of the crystalline basement of central Chile. *Journal of Petrology* **12**, 149–75.

GREEN, P. F., DUDDY, I. R., LASLETT, G. M., HEGARTY, K. A., GLEADOW, A. J. W. & LOVERING, J. F. 1989. Thermal annealing of fission-tracks in apatite 4. Quantitative modelling techniques and extension to geological timescales. *Chemical Geology* **79**, 155–82.

HOLLAND, T. J. B. & POWELL, R. 1998. An internally consistent thermodynamic data set for phases of petrological interest. *Journal of Metamorphic Geology* **16**, 309–43.

HOLLAND, T. J. B. & POWELL, R. 2003. Activity-composition relations for phases in petrological calculations: an asymmetric multicomponent formulation. *Contributions to Mineralogy and Petrology* **145**, 492–501.

HERVÉ, F. 1988. Late Palaeozoic subduction and accretion in Southern Chile. *Episodes* **11**, 183–8.

HERVÉ, F., FAÚNDEZ, V., CALDERÓN, M., MASSONNE, H.-J. & WILLNER, A. P. 2007. Metamorphic and plutonic basement complexes. In *The Geology of Chile* (eds T. Moreno & W. Gibbons), pp. 5–19. London: The Geological Society.

HURFORD, A. J. 1990. Standardization of fission-track dating calibration: recommended by the Fission-track Working Group of the I.U.G.S. Subcommission on Geochronology. *Chemical Geology (Isotope Geoscience Section)* **80**, 171–8.

HURFORD, A. J. & GREEN, P. F. 1983. The zeta age calibration of fission-track dating. *Isotope Geoscience* **1**, 285–317.

ISHIZUKA, O., YUASA, M. & UTO, K. 2002. Evidence of porphyry copper-type hydrothermal activity from a submerged remnant back-arc volcano of the Izu-Bonin arc: implication for the volcanotectonic history of back-arc seamounts. *Earth and Planetary Science Letters* **198**, 381–99.

IRWIN, J. J., GARCÍA, C., HERVÉ, F. & BROOK, M. 1988. Geology of part of a long-lived dynamic plate margin: the coastal cordillera of north-central Chile, latitude 30°51′-31°S. *Canadian Journal of Earth Sciences* **25**, 603–24.

KELLEY, S. P., ARNAUD, N. O. & TURNER, S. P. 1994. High spatial resolution ^{40}Ar-^{39}Ar investigations using an ultra-violet laser probe extraction technique. *Geochimica Cosmochimica Acta* **58**, 3519–25.

LEAKE, B. E., WOOLEY, A. R., ARPS, C. E. S., BIRCH, W. D., GILBERT, M. C., GRICE, J. D., HAWTHORNE, F. C., KATO, A., KISCH, H. J., KRIVOVICHEC, V. G., LINTHOUT, K., LAIRD, J., MANDARINO, J., MARESCH, W. V., NICKEL, E. H., ROCK, N. M. S., SCHUMACHER, J. C., SMITH, D. C., STEPHENSON, N. C. N., UNGARETTI, L., WHITTAKER, E. J. W. & YOUZHI, G. 1997. Nomenclature of amphiboles. Report of the subcommittee on amphiboles of International Mineralogical Association Committee on New Minerals and Mineral Names. *European Journal of Mineralogy* **9**, 623–51.

MASSONNE, H.-J. 1995*a*. Experimental and petrogenetic study of UHPM. In *Ultrahigh Pressure Metamorphism* (eds R. G. Coleman & X. Wang), pp. 33–95. Cambridge: Cambridge University Press.

MASSONNE, H.-J. 1995*b*. P-T evolution of metavolcanics from the southern Taunus mountains. In *Pre-Permian Geology of Central and Eastern Europe* (eds R. D. Dallmeyer, W. Franke, & K. Weber), pp. 132–7. Berlin-Heidelberg: Springer.

MASSONNE, H.-J. 1997. An improved thermodynamic solid solution model for natural white-micas and its application to the geothermobarometry of metamorphic rocks. *Geological Survey of Finland, Guide 46, Mineral equilibria and databases, Abstracts*, 49.

MASSONNE, H. J. & SZPURKA, Z. 1997. Thermodynamic properties of white-mica on the basis of high-pressure experiments in the systems K_2O-MgO-Al_2O_3-Si_2O-H_2O and K_2O-FeO-Al_2O_3-Si_2O-H_2O. *Lithos* **41**, 229–50.

MASSONNE, H.-J. & WILLNER, A. P. 2008. Phase relations and dehydration behaviour of psammopelite and mid-ocean ridge basalt at very-low-grade to low-grade metamorphic conditions. *European Journal of Mineralogy* **20**, 867–9.

MCDOUGALL, I. & HARRISON, T. M. 1999. *Geochronology and Thermochronology by the ^{40}Ar/^{39}Ar-Method*. Oxford: Oxford University Press, 269 pp.

MCDOWELL, D. S. & ELDERS, W. A. 1980. Authigenic layer silicate minerals in borehole Elmore 1, Salton Sea Geothermal Field, California, USA. *Contributions to Mineralogy and Petrology* **74**, 293–310.

MPODOZIS, C. & KAY, S. M. 1992. Late Palaeozoic to Triassic evolution of the Gondwana margin: evidence from Chilean Frontal Cordilleran batholiths (28°S to 31°S). *Geological Society of America Bulletin* **104**, 999–1014.

PANKHURST, R. J., MILLAR, I. L. & HERVÉ, F. 1996. A Permo-Carboniferous U-Pb age for part of the Guanta unit of the Elqui-Limarí Batholith at Rio Transito, Northern Chile. *Revista Geológica de Chile* **23**, 35–42.

PARADA, M. A., LOPEZ-ESCOBAR, L., OLIVEROS, V., FUENTES, F., MORATA, D., CALDERÓN, M., AGUIRRE, L., FÉRAUD, G., ESPINOZA, F., MORENO, H., FIGUEROA, O., MUNOZ BRAVO, J., TRONCOSO VÁSQUEZ, R. & STERN, C. R. 2007. Chapter 4 Andean magmatism. In *The Geology of Chile* (eds T. Moreno & W. Gibbons), pp. 115–46. London: The Geological Society.

POWELL, R. & HOLLAND, T. 1999. Relating formulations of the thermodynamics of mineral solid solutions: activity modeling of pyroxenes, amphiboles, and micas. *American Mineralogist* **84**, 1–14.

RAHN, M., BRANDON, M., BATT, G. E. & GARVER, J. I. 2004. A zero-damage model for fission-track annealing in zircon. *American Mineralogist* **89**, 473–84.

RAMÍREZ-SÁNCHEZ, E., DECKART, K. & HERVÉ, F. 2007. Significance of ^{40}Ar–^{39}Ar encapsulation ages of metapelites from late Palaeozoic metamorphic complexes of Aysén, Chile. *Geological Magazine* **145**, 389–96.

REBOLLEDO, S. & CHARRIER, R. 1994. Evolución del basamento Palaeozoico en el área de Punta Claditas, Región de Coquimbo, Chile (31–32°S). *Revista Geológica de Chile* **21**, 55–69.

REYNOLDS, P. H., BARR, S. M. & WHITE, C. E. 2009. Provenance of detrital muscovite in Cambrian Avalonia of Maritime Canada: ^{40}Ar/^{39}Ar ages and chemical compositions. *Canadian Journal of Earth Sciences* **46**, 169–80.

RICHTER, P., RING, U., WILLNER, A. P. & LEISS, B. 2007. Structural contacts in subduction complexes and their tectonic significance: the Late Palaeozoic coastal accretionary wedge of central Chile. *Journal of the Geological Society, London* **164**, 203–14.

RING, U., WILLNER, A. P., LAYER, P. W. & RICHTER, P. P. 2011. Jurassic to Early Cretaceous postaccretional sinistral transpression in north-central Chile (latitudes 31–32° S). *Geological Magazine*, **149**, 208–220.

RIVANO, S. & SEPÚLVEDA, P. 1983. Hallazgo de foraminíferos del Carbonífero Superior en la Formación Huentelauquén. *Revista Geológica de Chile* **19–20**, 25–35.

RIVANO, S. & SEPÚLVEDA, P. 1985. Las Calizas de la Formación Huenteauquén: Depósitos de aguas templadas a frías en el Carbonífero Superior-Pérmico Inferior. *Revista Geológica de Chile* **25–26**, 29–38.

TAGAMI, T., GALBRAITH, R. F., YAMADA, R. & LASLETT, G. M. 1998. Revised annealing kinetics of fission-tracks in zircon and geological implications. In *Advances in Fission-Track Geochronology* (eds P. Van den Haute & F. De Corte), pp. 99–112. Dordrecht: Kluwer Academic Publishers.

THIELE, R. & HERVÉ, F. 1984. Sedimentación y tectónica de antearco en los terrenos preandinos del Norte

Chico, Chile. *Revista Geológica de Chile* **22**, 61–75.

THOMSON, S. N. & HERVÉ, F. 2002. New time constraints for the age of metamorphism at the ancestral Pacific Gondwana margin of southern Chile (42–52° S). *Revista Geológica de Chile* **29**, 255–71.

THOMSON, S. N. & RING, U. 2006. Thermochronologic evaluation of postcollision extension in the Anatolide Orogen, western Turkey. Tectonics **25**, TC3005, doi:10.1029/2005TC001833, 20 pp.

UTO, K., ISHIZUKA, O., MATSUMOTO, A., KAMIOKA, H. & TOGASHI, S. 1997. Laser-heating $^{40}Ar/^{39}Ar$ dating system of the Geological Survey of Japan: system outlines and preliminary results. *Bulletin of the Geological Survey of Japan* **48**, 23–46.

VÁSQUEZ, P. & FRANZ, G. 2008. The Triassic Cobquecura Pluton (Central Chile): an example of a fayalite-bearing A-type intrusive massif at a continental margin. *Tectonophysics* **459**, 66–84.

VILLA, I. M. 1998. Isotopic closure. *Terra Nova* **10**, 42–7.

WILLNER, A. P. 2005. Pressure-temperature evolution of an Upper Palaeozoic paired metamorphic belt in Central Chile (34°-35°30′S). *Journal of Petrology* **46**, 1805–33.

WILLNER, A. P., GERDES, A. & MASSONNE, H.-J. 2008. History of crustal growth and recycling at the Pacific convergent margin of South America at latitudes 29°-36°S revealed by a U-Pb and Lu-Hf isotope study of detrital zircon from late Palaeozoic accretionary systems. *Chemical Geology* **253**, 114–29.

WILLNER, A. P., GLODNY, J., GERYA, T. V., GODOY, E. & MASSONNE, H.-J. 2004*a*. A counterclockwise PTt-path in high pressure-low temperature rocks from the Coastal Cordillera accretionary complex of South Central Chile: constraints for the earliest stage of subduction mass flow. *Lithos* **75**, 283–310.

WILLNER, A. P., HERVE, F. & MASSONNE, H.-J. 2000. Mineral chemistry and pressure-temperature evolution of two contrasting levels within an accretionary complex in the Chonos Metamorphic Complex, Southern Chile. *Journal of Petrology* **41**, 309–30.

WILLNER, A. P., WARTHO, J.-A., KRAMM, U. & PUCHKOV, V. N. 2004*b*. Laser ^{40}Ar–^{39}Ar ages of single detrital white-mica grains related to the exhumation of Neoproterozoic and Late Devonian high pressure rocks in the Southern Urals (Russia). *Geological Magazine* **141**, 161–72.

WILLNER, A. P., SEPÚLVEDA, F. A., HERVÉ, F., MASSONNE, H.-J. & SUDO, M. 2009. Conditions and timing of pumpellyite-actinolite facies metamorphism in the Early Mesozoic frontal accretionary prism of the Madre de Dios Archipelago (50°20′S; S-Chile). *Journal of Petrology* **50**, 2127–55.

WILLNER, A. P., THOMSON, S. N., KRÖNER, A., WARTHO, J. A., WIJBRANS, J & HERVÉ, F. 2005. Time markers for the evolution and exhumation history of a late Palaeozoic paired metamorphic belt in central Chile (34°-35°30′S). *Journal of Petrology* **46**, 1835–58.